

# APPLICATION OF ATTOSECOND TECHNIQUES TO CONDENSED MATTER SYSTEMS

DISSERTATION

Presented in Partial Fulfillment of the Requirements for the Degree Doctor of  
Philosophy in the Graduate School of The Ohio State University

By

Gregory J. Smith, M.Sc.

Graduate Program in Physics

The Ohio State University

2019

Dissertation Committee:

Louis F. DiMauro, Advisor

L. Robert Baker

Jay A. Gupta

Yuri V. Kovchegov

© Copyright by

Gregory J. Smith

2019

# Table of Contents

	Page
<b>List of Figures . . . . .</b>	iii
<b>1 Condensed Matter XUV Transient Absorption Experiments</b>	<b>1</b>
1.1 Statement of Contribution . . . . .	1
1.2 Introduction . . . . .	1
1.2.1 The Apparatus . . . . .	1
1.2.2 Attosecond Transient Absorption Spectroscopy (ATAS) . . . . .	4
1.3 Relative Contributions of Real and Imaginary Parts of $\tilde{n}$ . . . . .	5
1.4 Sample Requirements and Geometry . . . . .	9
1.5 Absorbance and Transient Absorbance Data Collection Methods . . . . .	10
1.6 The Supporting Nitride Membrane . . . . .	17
1.7 The Germanium Sample . . . . .	21
1.8 IR Pump Arm Considerations . . . . .	22
1.8.1 Calculation of IR Intensity at Focus . . . . .	23
1.8.2 Estimation of Excited Carrier Density . . . . .	24
1.8.3 The XUV-IR Overlap Integral . . . . .	27
1.9 Experimental Methods . . . . .	29
1.9.1 Finding XUV-IR spatial overlap . . . . .	29
1.9.2 Finding XUV-IR Temporal Overlap . . . . .	34
1.9.3 Optimization of IR Pump Parameters . . . . .	34
1.10 Summary . . . . .	46
<b>Chapters</b>	
<b>Bibliography</b>	<b>47</b>

# List of Figures

Figure	Page
1.1 Schematic of the Transient Absorption BeamLine (TABLE). Blue shaded region represents vacuum. BS: beam splitter, S: computer-controlled shutter, L: lens, I: iris, 2C: optics for two-color generation, HHG: high harmonic generation, F: metallic filter, EM: ellipsoidal mirror, HM: hole mirror, SH: sample holder, CF: long-pass color filter, WP: $\lambda/2$ waveplate, P: wire-grid polarizer, W: delay wedges, PD: photodiode and associated optics, DG: dispersive grating, MCP/P: micro-channel plate and phosphor. . . . .	2
1.2 Schematic of an attosecond transient absorption spectroscopy (ATAS) experiment. An IR laser pulse excites electrons in the material, driving them across the band-gap. An XUV pulse passes through the sample after a delay $\Delta t$ . The measured XUV absorbance is sensitive to electronic populations and states. Figure taken from [12]. . . . .	3
1.3 Normal and non-normal incident geometries. <b>a)</b> Normal incidence geometry showing Fresnel coefficients $R_F$ , $T_F$ for interfaces and total transmission $T$ and reflectance $R$ for a slab of thickness $L$ . Figure recreated from [10]. <b>b)</b> Non-normal geometry showing definitions of angles $\theta_i$ , $\theta_r$ and $\theta_t$ with respect to each interface. . . . .	5
1.4 Consequences of ignoring the real part of $\tilde{n}$ when calculating the transmission $T$ of a thin sample. Top panel: complex refractive index of silicon using the notation from Eq. (1.1). The Si $L$ -edge absorption feature is visible near 100 eV. Data from [6]. Bottom panel: relative error in $T$ , as defined in Eq. (1.8), introduced by ignoring the contribution of $\text{Re}(\tilde{n})$ . An infinite number of bounces (e.g., Eq. (1.6)) is assumed. . . . .	6
1.5 Calculated XUV transmission of various materials. Data from [6]. . . . .	9
1.6 Calculated XUV transmission of various metallic filters. Data from [6]. . . . .	11

1.7	Schematic of competing raster methods, shown in the sample's reference frame. The clear aperture of the sample is represented by the interior of the black square. The laser propagation direction is out of the page. The laser focal spots are shown as red circles, and the movement of the sample holder relative to the laser focus is indicated by arrows. A $200 \mu\text{m}$ border exists between the raster array and the perimeter of the sample's clear aperture. This diagram is to scale for a $1 \times 1 \text{ mm}^2$ clear aperture sample, a $60 \mu\text{m}$ diameter IR focal spot and a $200 \mu\text{m}$ step size. . . . .	11
1.8	XUV transmission measurements of Al metallic filter and silicon nitride membrane. Left panel: normalized XUV counts for i) unfiltered HHG signal, ii) HHG going through a $200 \text{ nm}$ Al filter and iii) HHG going through a $200 \text{ nm}$ Al filter and $30 \text{ nm}$ of silicon nitride. Counts are scaled by the Jacobian. Right panel: transmission curves obtained from the left panel's data. Also shown are literature values for $20 \text{ nm}$ of silicon nitride and $200 \text{ nm}$ of Al with two $4 \text{ nm}$ oxide layers [6]. Multilayer interference is not taken into account. Oscillations in measured transmission are numerical artifacts which will be discussed in the text. . . . .	15
1.9	XUV transmission map of $30 \text{ nm}$ silicone nitride freestanding membrane. Left panel: integrated XUV counts in the range $30 - 34 \text{ eV}$ . Sample holder motor positions are indicated by x- and y-positions. Right panel: histogram of logarithmic deviation of counts from the average. Dashed line shows a normal distribution. . . . .	16
1.10	Cartoon showing the cross section of the free standing sample heterostructure. A $500 \mu\text{m}$ thick Si frame supports a freestanding $30 \text{ nm}$ low stress silicon nitride membrane (Norcada QX7300X), upon which $100 \text{ nm}$ of germanium has been deposited. The Si frame has a $3 \times 3 \text{ mm}^2$ square clear aperture and a $7.5 \times 7.5 \text{ mm}^2$ square external dimension. The taper of the Si frame thickness along the perimeter of the clear aperture forms a knife edge. In an ATAS experiment, the XUV and IR pulses propagate from the top to bottom of the figure. . . . .	16
1.11	Band structure and orbital character of germanium. Purple arrows indicate XUV-induced transitions from the $3d$ core levels to the valence bands. Red arrow indicates IR-induced transition across the direct band gap. Figure adapted from [15]. . . . .	20
1.12	Measured ground absorbance $A$ of a $100 \text{ nm}$ Ge film on a $30 \text{ nm}$ silicon nitride membrane. The contribution of the membrane has been subtracted. Blue line is the measured absorbance $A$ . The red dashed line shows the result of numerical filtering to eliminate numerical artifacts (described in main text). . . . .	20
1.13	Left panel: spatial mapping of integrated XUV counts ( $30 - 34 \text{ eV}$ ) of a $100 \text{ nm}$ Ge + $30 \text{ nm}$ silicon nitride sample. Right panel: normalized histogram of counts $c$ from the left panel. . . . .	21

1.14 Numerical propagation of the IR ( $\lambda=1500$ nm) beam through the pump arm. Beam path layout follows Fig. 1.1. Each panel shows the intensity of the beam as the beam propagates towards the focus. The first panel shows the measured intensity (Electrophysics PV320 thermal camera), all other panels are calculations. The arrows on the lineout indicate the FWHM. All calculations are for vacuum ( $n = 1$ ). See text for details. . . . .	23
1.15 XUV-IR overlap function, as defined in Eq. (1.19), calculated using the numerical simulation results of Fig. 1.14 and a Gaussian XUV beam with a $6\ \mu\text{m}$ waist. The result has been normalized to perfect overlap, $a_{max}$ . . . . .	25
1.16 Schematic of XUV knife edge measurement. EM: ellipsoidal mirror, $z_0$ : XUV focal plane. . . . .	30
1.17 A typical XUV knife edge measurement near the focal plane. The sample motor position is $k = 11.0000$ mm. A fit to equation Eq. (1.23) yields a beam waist of $10.82\ \mu\text{m}$ at this position. . . . .	30
1.18 Evolution of XUV beam waist as a function of propagation direction, $z$ . The Rayleigh range $z_R$ and beam waist $w_0$ are extracted from the fit to Eq. (1.22). . . . .	31
1.19 <i>In-situ</i> imaging of the samples within the target chamber. Left: optical setup for <i>in-situ</i> imaging of samples. C: Si CCD camera, HM: hole mirror, SH: sample holder, FM: translatable silver mirror, L: lens. Right: false color image showing the sample holder with a $3 \times 3$ grid of 5 mm diameter clear apertures. Samples are held in a clamshell design centered in the clear apertures and are backlit using a flashlight. . . . .	35
1.20 False color images showing laser drilled freestanding membranes. Left: pristine 260 nm thick Si membrane (Norcada). Middle: same sample, after performing an IR power scan that exceeded the membrane's damage threshold. A $<200\ \mu\text{m}$ hole is visible as a cluster of bright pixels near the center of the membrane. Right: 30 nm SiN membrane after a similar power scan showing a "popped" membrane. The ragged edges near the clear aperture of the frame are all that remain of the membrane. For all images, the apparent brightness gradient across the samples is caused by inconsistent backlighting. Images were taken using the optical setup shown in the left panel of Fig. 1.19. . . . .	35
1.21 Laser damaged 200 nm silicon membrane samples. Left panel: XUV map of pristine Si before being exposed to IR laser. Higher transmission is indicated by brighter colors. Sample is rotated approximately 30 degrees relative to motor axes. Center panel: XUV map of damaged sample after being pumped with $\approx 65\ \mu\text{J}$ of $\lambda = 1500$ nm at 1 kHz rep. rate in two locations. Damage occurred within the first camera exposure (2 seconds) and propagated to regions that were not exposed to the laser. Right panel: microscope image of damaged sample (beige) showing large sections of missing material (white). Red circles in all three pictures indicate the two locations that were exposed to IR laser light. . . . .	36

1.22	1 kHz fixed-delay ATAS measurements on 100 nm Ge using a $\lambda = 1450$ nm excitation pulse. See text for details.	38
(a)	$\tau \approx 0$ fs, PE = 1.03 $\mu$ J.	38
(b)	$\tau \approx 0$ fs, PE = 1.43 $\mu$ J.	38
(c)	$\tau = -\infty$ , PE = 1.03 $\mu$ J.	38
(d)	$\tau = -\infty$ , PE = 1.43 $\mu$ J.	38
(e)	PE = 1.03 $\mu$ J.	38
(f)	PE = 1.43 $\mu$ J.	38
1.23	1 kHz ATAS measurements in Ge using a $\lambda = 1450$ nm excitation pulse. Fig. 1.23a: fixed-delay ATAS measurements with a pulse energy of 1.75 $\mu$ J. Fig. 1.23b: Pulse energy scaling at overlap of 1 kHz measurements. Figs. 1.23c to 1.23f: delay scans at 1 kHz. Figs. 1.23c and 1.23d: raw delay scan data. Figs. 1.23e and 1.23f: rolling average of the raw data with a 65 fs window (20 delay points). The left panel on each spectrogram shows the ground state spectrum $S_{gs}(E)$ . See text for details.	39
(a)	$\tau \approx 0$ fs, PE = 1.75 $\mu$ J.	39
(b)	PE scaling at $\tau \approx 0$ fs.	39
(c)	PE = 1.43 $\mu$ J.	39
(d)	PE = 1.75 $\mu$ J.	39
(e)	PE = 1.43 $\mu$ J (rolling average).	39
(f)	PE = 1.75 $\mu$ J (rolling average).	39
1.24	500 Hz ATAS measurements in Ge using a $\lambda = 1450$ nm, 1.67 $\mu$ J excitation pulse. Each delay curve is an average of 104 identical measurements. The sample shows no delay dependance within the uncertainty of the measurement.	40
1.25	125 Hz ATAS measurements in Ge using a $\lambda = 1450$ nm, 2.64 $\mu$ J excitation pulse. Each lineout represents the average of 394 measurements. See text for details.	40
1.26	125 Hz delay scan in Ge using a $\lambda = 1450$ nm, $2.74 \pm 0.35$ $\mu$ J excitation pulse. This is an average of 3 repeated measurements. See text for details..	41
1.27	125 vs. 250 Hz measurements at $\lambda = 1430$ nm.	41
(a)	125 Hz ( $M = 6$ )	41
(b)	250 Hz ( $M = 2$ )	41
1.28	Pulse energy scan of 100 nm germanium sample near temporal overlap using a $\lambda = 1430$ nm excitation pulse. Left panel shows the average ground state spectrum, $S_{gs}(E)$ that results from two-color generation. Right panel shows the change in absorbance, $\Delta A(E, PE)$ , as a function of pulse energy, PE. Data shown in this figure is the average of 20 identical measurements: individual datasets were background subtracted and normalized for exposure time before being averaged; no additional data processing was performed on this dataset. See text for details.	44
1.29	Average of 50 ATAS experiments using optimized experimental parameters. No corrections have been made to the data. See text for details.	44

# Chapter 1

## CONDENSED MATTER XUV TRANSIENT ABSORPTION EXPERIMENTS

### 1.1 Statement of Contribution

This experiment uses home-made equipment consisting of a XUV-IR Mach-Zhender interferometer, a bright XUV light source, a target chamber and an XUV photon spectrometer. The entire apparatus was designed and built by Gregory Smith and Stephen Hageman. Dietrich Kiesewetter helped test and improve the stability of the interferometer. The LabView software controlling the spectrometer's detector and shutters was programmed by Kent Talbert. The vacuum system's safety system was designed and programmed by Andrew Piper. The germanium samples were grown by Dr. Yaguo Tang. Transient absorption experiments were done by Gregory Smith and Stephen Hageman. Analysis presented in this document was done by Gregory Smith. Further details on the apparatus and the relevant physics will be discussed in the main dissertation.

### 1.2 Introduction

#### 1.2.1 The Apparatus

We generate extreme ultraviolet (XUV) light using an extremely non-linear process called *high harmonic generation* (HHG). Briefly, the XUV light source can be thought of as a frequency comb spanning from  $\sim 20$  eV to  $\sim 50 - 150$  eV. Depending on the generation

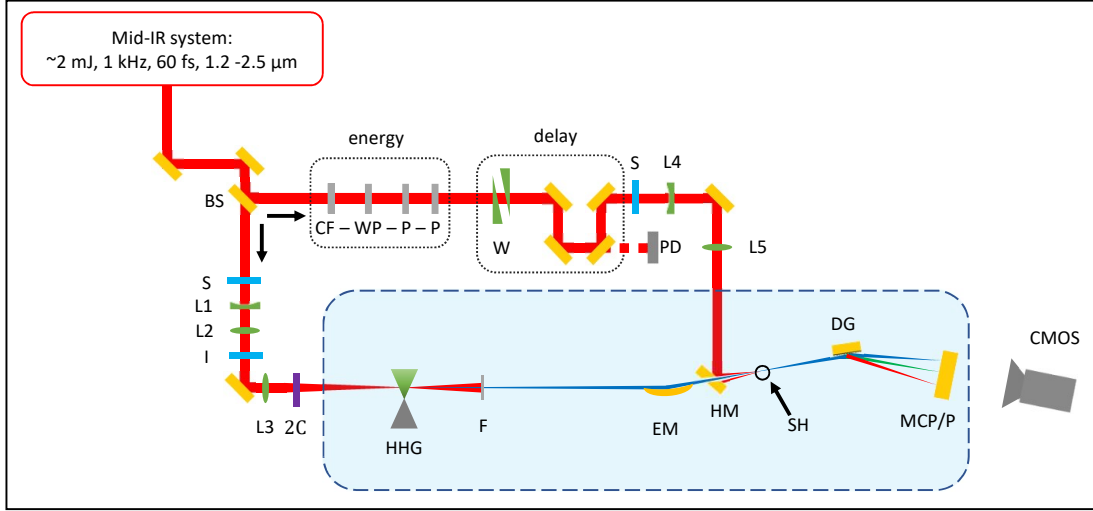


Figure 1.1: Schematic of the Transient Absorption BeamLine (TABLE). Blue shaded region represents vacuum. BS: beam splitter, S: computer-controlled shutter, L: lens, I: iris, 2C: optics for two-color generation, HHG: high harmonic generation, F: metallic filter, EM: ellipsoidal mirror, HM: hole mirror, SH: sample holder, CF: long-pass color filter, WP:  $\lambda/2$  waveplate, P: wire-grid polarizer, W: delay wedges, PD: photodiode and associated optics, DG: dispersive grating, MCP/P: micro-channel plate and phosphor.

conditions, the separation between the teeth of the frequency comb is either  $\omega$  or  $2\omega$ , where  $\omega$  is the frequency of our laser light. In the time domain, the XUV is a train of attosecond bursts of broadband light with an envelope of  $\sim 50$  fs. This XUV light is phase locked to the field that generated it, so it this process can be used within an interferometer with sub-cycle stability. Due to the ionizing nature of XUV light, the entire experiment must be performed under vacuum.

The experiment is powered by a commercial mid-IR laser system (Spectra Physics Spitfire ACE), which delivers 12 mJ of 800 nm light at a variable 100 – 1,000 Hz repetition rate,  $\sim 65$  fs duration. This light is sent into a commercial optical parametric amplifier (Light Conversion HE TOPAS Prime), which converts it to longer wavelengths ( $1.2 - 2.5 \mu\text{m}$ ,  $\approx 2$  mJ) using a non-linear process while roughly maintaining pulse duration. The output of the TOPAS is routed into the *transient absorption beamline* (TABLE), shown in Fig. 1.1. The TABLE is a Mach-Zhender interferometer with a HHG source in the generation arm and energy & delay controls in the pump arm. A beam splitter (BS) delivers the bulk of

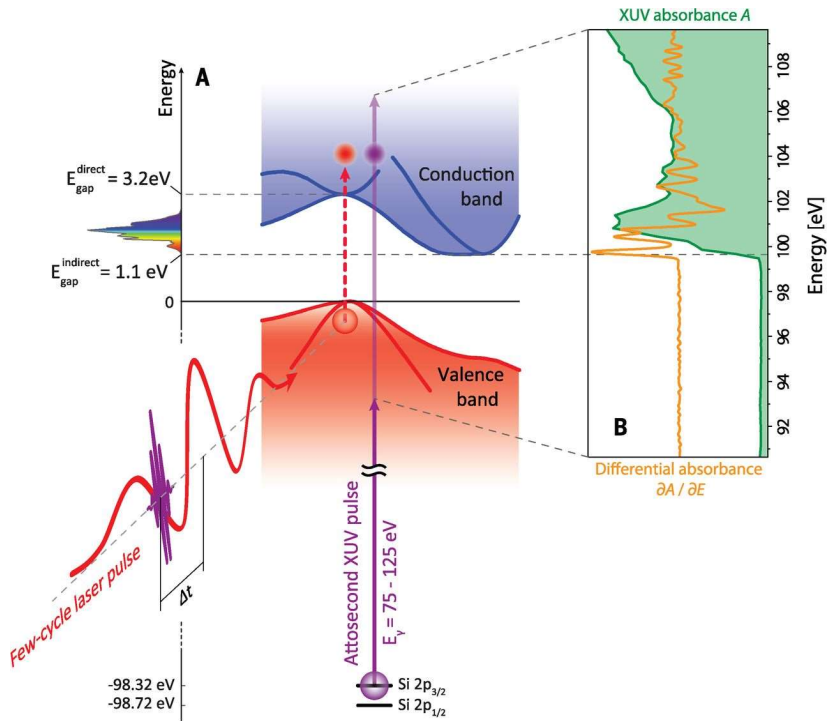


Figure 1.2: Schematic of an attosecond transient absorption spectroscopy (ATAS) experiment. An IR laser pulse excites electrons in the material, driving them across the band-gap. An XUV pulse passes through the sample after a delay  $\Delta t$ . The measured XUV absorbance is sensitive to electronic populations and states. Figure taken from [12].

the pulse energy (96%) to the generation arm of the interferometer, which contains the HHG source and specialized XUV focusing optics. A small percentage of TOPAS’s pulse energy goes to the pump arm, which contains optics to control the pulse energy, relative delay between the two arms, and focusing optics. The pump arm is routed into the vacuum system, where a silvered hole mirror (HM) combines the two arms of the interferometer in a collinear fashion. Note that the HM represents the end of the interferometer. This optic is designed to allow the XUV light to pass through a clear aperture on the backside of the HM while the pump arm’s IR light reflects off the front face. The interferometer is aligned so that both arms have a common focus in the target chamber at the sample holder (SH). A home-built photon spectrometer positioned behind the sample records the transmitted XUV spectrum.

### 1.2.2 Attosecond Transient Absorption Spectroscopy (ATAS)

The basic concept of an *attosecond transient absorption spectroscopy* (ATAS) experiment is shown in Fig. 1.2. In this experiment, a sample is placed at the combined XUV/IR focus in a transmission (normal) geometry. An XUV photon spectrometer is placed behind the sample and the transmitted XUV spectrum  $S$  is measured as a function of XUV-IR delay. The IR light is not measured by the spectrometer.

Fundamentally, changes in photoabsorption correspond to electron and phonon dynamics in the sample. In condensed matter materials, these processes occur on the picosecond ( $10^{-12}$  s), femtosecond ( $10^{-15}$  s) and even attosecond ( $10^{-18}$  s) time scales [4, 12, 14, 15]. At XUV energies, photons drive electronic transitions from a core-level state to one near the Fermi level, which requires electron population in the initial state and a vacancy in the final state. Because the initial state is tens or even hundreds of eV below the bandgap, it is shielded from the external IR field. The final states, being closer to the Fermi level, enjoy no such shielding. Therefore they can be distorted by the external IR field, and the electron population can be transferred between these states in response to the IR field. After an initial IR excitation, electrons relax via different scattering channels, including with other electrons or phonon modes with longer lifetimes. Provided the dipole selection rules allow

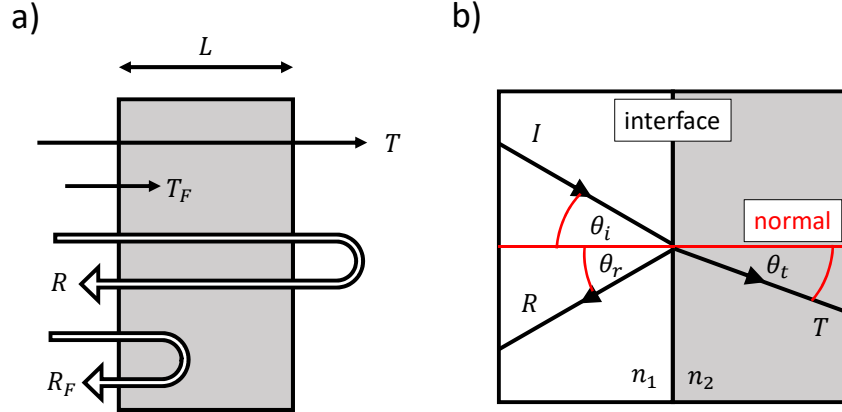


Figure 1.3: Normal and non-normal incident geometries. a) Normal incidence geometry showing Fresnel coefficients  $R_F$ ,  $T_F$  for interfaces and total transmission  $T$  and reflectance  $R$  for a slab of thickness  $L$ . Figure recreated from [10]. b) Non-normal geometry showing definitions of angles  $\theta_i$ ,  $\theta_r$  and  $\theta_t$  with respect to each interface.

it, the photoabsorption spectrum is sensitive to all of these dynamics. Thus by measuring the XUV spectrum as a function of XUV-IR delay, we can track the electronic and phononic response of a sample to an ultrafast IR excitation.

This chapter will discuss the experimental considerations and methods associated with an ATAS experiment.

### 1.3 Relative Contributions of Real and Imaginary Parts of $\tilde{n}$

In a transient absorption experiment, we measure the transmission  $T$  of a sample in response to excitation by an external field. Generally speaking,  $T$  depends on both parts of the complex refractive index:  $\tilde{n} = n + ik$ . However, in a normal transmission geometry it turns out that the contribution of  $\text{Im}(\tilde{n})$  dominates the measured signal, and to a good approximation the role of  $\text{Re}(\tilde{n})$  can be ignored. Note that in a non-normal reflection geometry, both parts of  $\tilde{n}$  make significant contributions to the measured signal. In the following discussion we will analyze the Fresnel equations to see why this is the case. This section will draw from arguments made in reference [10].

First, we consider the normal geometry shown in the left panel of Fig. 1.3. We write

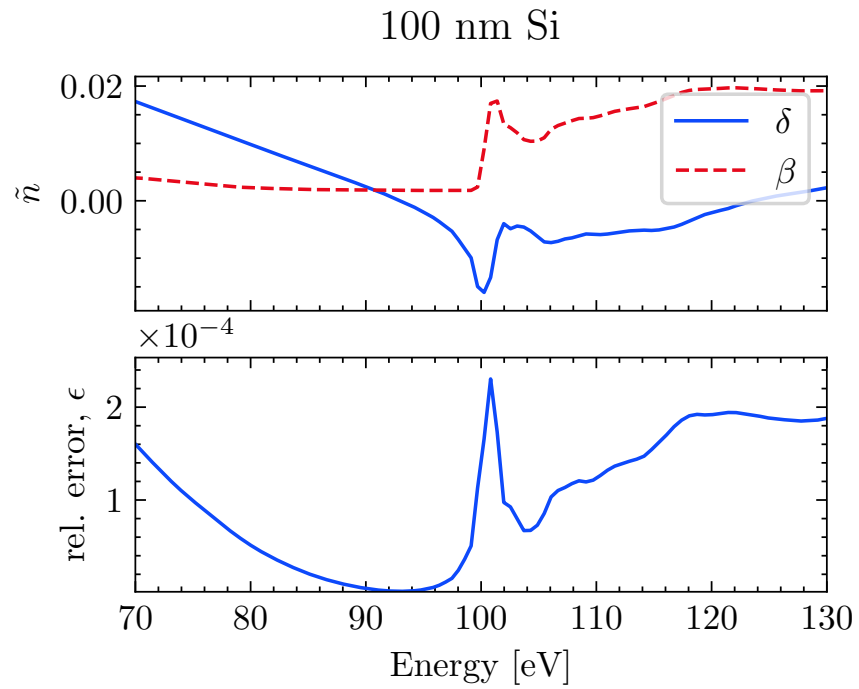


Figure 1.4: Consequences of ignoring the real part of  $\tilde{n}$  when calculating the transmission  $T$  of a thin sample. Top panel: complex refractive index of silicon using the notation from Eq. (1.1). The Si  $L$ -edge absorption feature is visible near 100 eV. Data from [6]. Bottom panel: relative error in  $T$ , as defined in Eq. (1.8), introduced by ignoring the contribution of  $\text{Re}(\tilde{n})$ . An infinite number of bounces (e.g., Eq. (1.6)) is assumed.

the complex index of refraction in the following form:

$$\begin{aligned}\tilde{n} &= n - ik \\ &= (1 - \delta) - i\beta\end{aligned}\tag{1.1}$$

The Fresnel coefficients  $R_F$  and  $T_F$  describe the interface reflectance and transmittance and depend on both parts of the complex index  $\tilde{n}$ . For normal incidence, they are:

$$\begin{aligned}R_F &= \left| \frac{n - ik - 1}{n - ik + 1} \right|^2 \\ T_F &= \frac{4n}{|n - ik + 1|^2}\end{aligned}\tag{1.2}$$

Absorption in the bulk is described via the absorption length  $\alpha$ :

$$\alpha = 4\pi k/\lambda\tag{1.3}$$

Ignoring interface effects, the transmisison through the bulk is:

$$T_{\text{bulk}} = \exp(-\alpha L)\tag{1.4}$$

Note that  $\alpha$  and  $T_{\text{bulk}}$  only depend on  $k$ .

The total reflectance  $R$  and transmission  $T$  are the result of interface effects plus bulk effects. We must consider the case where the detected light is the result of multiple reflections within the sample. Neglecting interference, we consider the case of  $2N$  bounces where the laser's coherence length is less than the thickness of the bulk. In this case, the sum is incoherent with the expressions for  $T$  and  $R$  given by:

$$\begin{aligned}R &= R_F + R_F T_F^2 T_{\text{bulk}}^2 \sum_{m=0}^N [R_F T_{\text{bulk}}]^{2m} \\ T &= T_F^2 T_{\text{bulk}} \sum_{m=0}^N [R_F T_{\text{bulk}}]^{2m}\end{aligned}\tag{1.5}$$

For the case of an infinite number of bounces, Eq. (1.5) simplifies to:

$$\begin{aligned}R &= R_F + \frac{R_F T_F^2 T_{\text{bulk}}^2}{1 - R_F^2 T_{\text{bulk}}^2} \\ T &= \frac{T_F^2 T_{\text{bulk}}}{1 - R_F^2 T_{\text{bulk}}^2},\end{aligned}\tag{1.6}$$

whereas if only a single bounce occurs, Eq. (1.5) reduces to:

$$\begin{aligned} R &= R_F + R_F T_F^2 T_{\text{bulk}}^2 \\ T &= T_F^2 T_{\text{bulk}} \end{aligned} \tag{1.7}$$

We now consider the fractional error introduced by ignoring the interface effects described by  $T_F$  and  $R_F$ . That is, what would happen if we assume that the interfaces have no effect on the transmitted intensity? We introduce the relative error  $\epsilon$  made by ignoring the Fresnel coefficients of Eq. (1.6):

$$\epsilon \equiv \frac{T_{\text{bulk}}}{T} - 1 \tag{1.8}$$

As an example, consider a 100 nm thick Si sample measured in transmission near the Si *L*-edge (about 100 eV), as shown in Fig. 1.4. The relative error is in the range of one part in  $10^4$  to  $10^5$ , well below our experimental detection limit. Silicon was chosen due to its data availability above and below the absorption edge, but this behavior should hold for all materials in normal transmission.

The real part of the complex index becomes important when the sample isn't normal to the beam, as shown in the right panel of Fig. 1.3. In this case, the Fresnel equations are a bit messier:

$$\begin{aligned} R_s &= \left| \frac{\tilde{n}_1 \cos \theta_i - \tilde{n}_2 \cos \theta_t}{\tilde{n}_1 \cos \theta_i + \tilde{n}_2 \cos \theta_t} \right|^2 \\ R_p &= \left| \frac{\tilde{n}_1 \cos \theta_t - \tilde{n}_2 \cos \theta_i}{\tilde{n}_1 \cos \theta_t + \tilde{n}_2 \cos \theta_i} \right|^2 \end{aligned} \tag{1.9}$$

$$T_s = 1 - R_s$$

$$T_p = 1 - R_p$$

Here, the subscripts *s* and *p* denote the polarization relative to the surface normal. For a sample in vacuum,  $\tilde{n}_1 = 1$  and  $\tilde{n}_2$  is the index of the sample. We can extract the relevant physics without any additional manipulation of Eq. (1.9). Right away, we can see that unlike Eq. (1.2), Eq. (1.9) is symmetric in the real and imaginary parts of the sample's complex index,  $\tilde{n}_2$ . In the limit of a thick slab, ( $L \gg \alpha$ ), the light is attenuated before it can reflect off the back surface and we have  $T \rightarrow 0$  and  $R \rightarrow R_{s,p}$ . That is, the only contributions to the

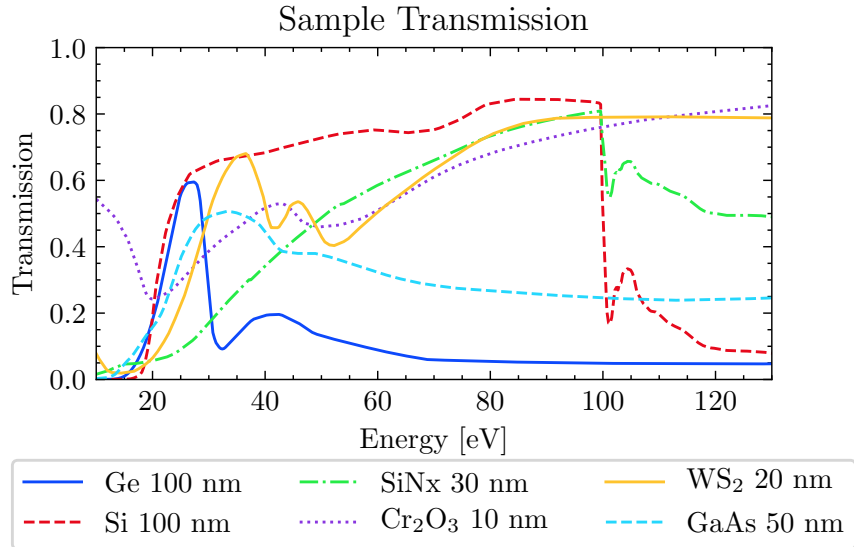


Figure 1.5: Calculated XUV transmission of various materials. Data from [6].

reflected intensity are from the interface and possibly the sample volume within  $z \approx 1/\alpha$  of the interface. As a result, both parts of  $\tilde{n}_2$  will make significant contributions to the reflected intensity. This geometry is common in transient reflection-absorption experiments [3, 8].

## 1.4 Sample Requirements and Geometry

There are several sample requirements for a successful condensed matter transient absorption experiment. First and foremost, the sample needs to have an absorption edge within the bandwidth of the XUV source. Second, the material must be the correct thickness for a transmission measurement, given the capabilities of the XUV light source and detector. If the material is too thick, the ground state will absorb most of the XUV flux and the recorded spectrum will be too close to the noise floor of the apparatus. If it is too thin, the laser-induced change of the ground state (on the order of 1 – 10%) will be lost in the noise. As a general guideline, a sample that absorbs 50% at the spectral feature of interest provides a good compromise between these conflicting requirements. Fig. 1.5 shows the expected transmission of several materials, calculated from the atomic scattering factors

[6]. We can see that a typical sample will be on the order of 10 - 200 nm thick, depending on the material.

Another upper bound for sample thickness comes from material dispersion. In any material, the XUV light ( $n_{\text{IR}} \sim 1$ ) will outpace the IR light ( $n_{\text{IR}} > 1$ ). This effect can be significant even for ultrathin films. In order to keep the phase slippage between the XUV and IR light below half an IR period, the sample thickness  $h$  must obey the following relationship:

$$L \leq \frac{1}{2} \frac{\lambda_{\text{IR}}}{n_{\text{IR}} - n_{\text{XUV}}} \quad (1.10)$$

For germanium excited with  $\lambda_{\text{IR}} = 1430$  nm and probed with 30 eV XUV at the  $M_{4,5}$  edge,  $n_{\text{IR}} = 4.2481$  [11] and  $n_{\text{XUV}} = 0.992536$  [6], which gives a maximum thickness of 220 nm.

Next, the sample needs to be excitable using laser sources present in our lab (i.e., ultrafast pulses with wavelengths between 800 nm and a couple of microns). To minimize the slow build up of heat (on the order of seconds) and laser-induced damage, the sample needs to be rastered through the laser focus as the experiment is performed. This rastering method necessitates both a large clear aperture ( $\sim 1 \text{ mm}^2 - 1 \text{ cm}^2$ ) and good sample uniformity. Samples that meet the above thickness and clear aperture requirements are extremely delicate, with thicknesses between 5,000 and 100,000 times smaller than their freestanding lateral dimensions. As such, one should expect most samples to break before, during and after measurements, so a successful experiment will have a materials pipeline that is capable of producing multiple, consistent samples in a short time frame.

## 1.5 Absorbance and Transient Absorbance Data Collection Methods

The *absorbance*<sup>1</sup>  $A$  is defined as the negative logarithm of the transmission  $T$ :

$$A(E) = -\log_{10}(T) = -\log_{10}\left(\frac{S_{gs}(E)}{S_{vac}(E)}\right). \quad (1.11)$$

In Eq. (1.11),  $S_{gs}(E)$  is the XUV spectrum transmitted by the sample in its ground state

<sup>1</sup>The terms absorbance and optical density are often used interchangably.

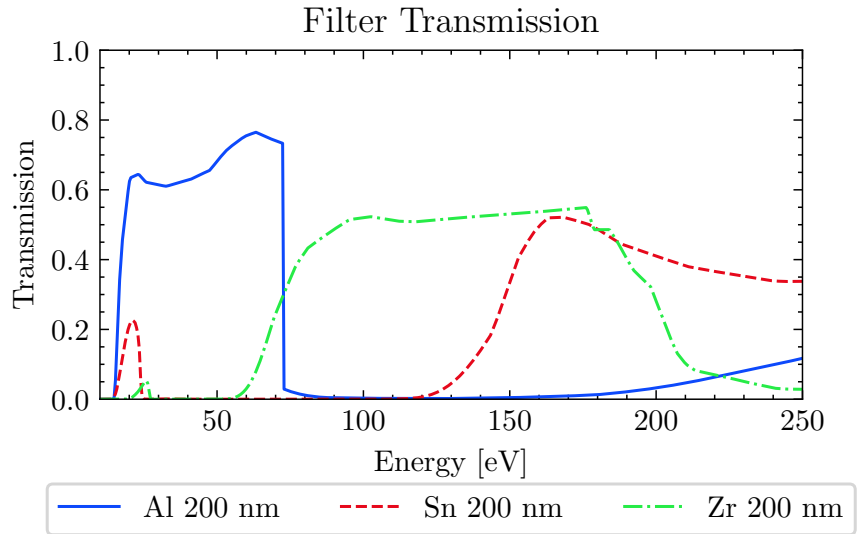


Figure 1.6: Calculated XUV transmission of various metallic filters. Data from [6].

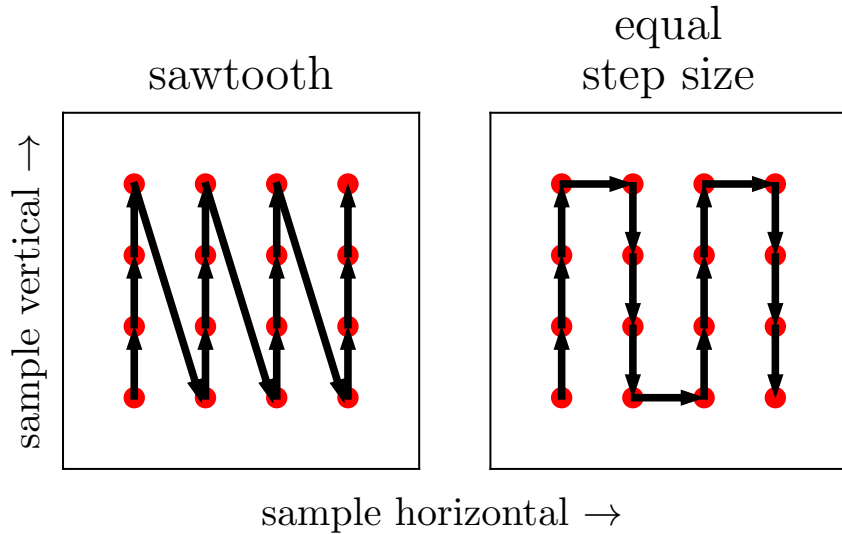


Figure 1.7: Schematic of competing raster methods, shown in the sample's reference frame. The clear aperture of the sample is represented by the interior of the black square. The laser propagation direction is out of the page. The laser focal spots are shown as red circles, and the movement of the sample holder relative to the laser focus is indicated by arrows. A 200  $\mu\text{m}$  border exists between the raster array and the perimeter of the sample's clear aperture. This diagram is to scale for a  $1 \times 1 \text{ mm}^2$  clear aperture sample, a 60  $\mu\text{m}$  diameter IR focal spot and a 200  $\mu\text{m}$  step size.

and  $S_{vac}(E)$  is the spectrum without the sample present. Therefore we can measure the sample's ground state absorbance by measuring the harmonic spectrum with and without the sample in the XUV beam.

The *change in absorbance*  $\Delta A$  between the ground and laser-induced excited state is therefore:

$$\begin{aligned}\Delta A(E, \tau) &= A_{\text{sig}}(E, \tau) - A_{\text{gs}}(E) \\ &= -\log_{10} \left( \frac{S_{\text{sig}}(E, \tau)}{S_{\text{vac}}(E)} \right) - \log_{10} \left( \frac{S_{\text{gs}}(E)}{S_{\text{vac}}(E)} \right) \\ &= -\log_{10} \left( \frac{S_{\text{sig}}(E, \tau)}{S_{\text{gs}}(E)} \right).\end{aligned}\quad (1.12)$$

In Eq. (1.12), the signal spectrum  $S_{\text{sig}}(E, \tau)$  is the spectra that results from an IR pulse hitting the sample, followed by an XUV pulse after a delay of  $\tau \equiv t_{\text{XUV}} - t_{\text{IR}}$ . Note that negative delays mean the XUV arrives at the sample before the IR and zero delay indicates temporal overlap of the two pulses. It is assumed that a delay of negative infinity is equivalent to a ground state measurement:  $S_{\text{sig}}(E, \tau = -\infty) = S_{\text{gs}}$ .

An ATAS experiment is simply a collection of recorded spectra taken over a range of delay points with otherwise identical experimental conditions. However, we have implemented several techniques to improve the fidelity of our data.

HHG is an extremely inefficient process, with a IR-to-XUV conversion ratio on the order of  $10^{-6}$ . After the generation cell, the leftover IR light must be blocked or it will destroy any sample located downstream. We use a thin metallic filter (Al, Zr or Sn), placed about 1 m after the harmonic source, which acts as a bandpass filter, blocking the IR field and passing a portion of the XUV spectrum. The choice of filter is dictated by the photon energy range of the spectral features we want to study. For more detail, see Fig. 1.6.

As an extremely nonlinear process, HHG's conversion efficiency is highly dependent on the input laser pointing, peak power, pulse duration, spatial mode, etc. – all of which are affected by laboratory environmental conditions and the activity of other group members within our lab complex. As a result, even during “ideal” experimental conditions, the total harmonic yield drifts slowly throughout the course of the experiment. To minimize the effect of this slow drift, we take a ground state spectrum for each delay point.

A computer-controlled home-built shutter system blocks the IR laser in the pump arm between measurements (S in Fig. 1.1). Taking back-to-back ground and excited state spectra significantly lowers the harmonic stability requirements; we require stability on the order of twice the exposure time (several seconds), rather than the entire experimental run (several hours).

Our spectrometer’s CMOS camera has a bit depth of 16, corresponding to a maximum value of  $2^{16} - 1 = 65,535$  counts before saturation. The exposure time is set so that the amplitude of the brightest harmonic on the detector is about 10% below this limit, which allows for an upward drift in harmonic yield to occur without invalidating the dataset. An exposure time of 3 seconds is typical for a 200 nm Al filter with a 100 nm Ge sample at 125 Hz (375 laser shots), an MCP voltage of +2200 VDC, and  $2 \times 2$  camera pixel binning.

Although the Spitfire laser system has a maximum repetition rate of 1 kHz, we perform solid state ATAS experiments at a much lower rate (125 or 250 Hz) by adjusting the amplifier’s Pockels cell firing rate. The lower repetition rate allows the sample to more fully relax between laser shots, reducing the effects of millisecond thermal processes on our measurements. It also reduces the average power on the sample for a given pulse energy, which lowers the steady state temperature of the sample. On the other hand, it allows us to increase the pulse energy while maintaining a constant average power on the sample.

During the experiment, the sample is rastered across the focus to reduce any deleterious effects of long term uninterrupted laser exposure. During motor movement, the IR beam is blocked with a shutter but the relatively weak XUV beam is allowed to remain on the sample. Each pair of measurements (ground state, excited state) in a delay scan has a unique position on the sample. Typical step sizes are 200  $\mu\text{m}$ , which is larger than the measured XUV spot size of  $\sim 12 \mu\text{m}$  and the IR spot size of  $\sim 35 \mu\text{m}$ . Two raster schemes are schematically shown in Fig. 1.7. The method shown in the left panel produces a sawtooth pattern on the sample. This method gives very accurate positioning, as the vertical motor is almost always approaching the final position from the same direction. However, the diagonal steps are  $\sqrt{N^2 + 1}$  times longer than the vertical steps, where  $N$  is the number of vertical steps in the pattern. As a result, there is a bimodal distribution of motor transit

times between measurements. If the sample is not fully relaxed between motor movements, this will lead to an inconsistent measurement of the ground state  $S_{\text{gs}}(E)$ . Additionally, if the sample is heated by the laser outside of the raster step size, then the average distance between points can affect the measurement of the ground state. The method shown in the right panel alleviates both problems by requiring equal step sizes. Measurements presented in this work were acquired using the method shown in the right panel.

Before measuring a sample's response for the first time, or after a major optical alignment, an XUV transmission map of the sample must be created. Creating this map serves two purposes: it verifies sample XUV absorption uniformity and it determines the motor coordinates of the sample's clear aperture. To avoid edge effects, the edges of the raster area are chosen to be 200  $\mu\text{m}$  away from the edge of the clear aperture (see Fig. 1.7).

The next step is a measurement of the sample's absorbance  $A$ . Per Eq. (1.11), this is achieved by taking spectra with ( $S_{\text{gs}}$ ) and without ( $S_{\text{vac}}$ ) the sample in the XUV beam. These measurements are recorded as quickly as the motors will permit, <10 seconds between spectra to minimize harmonic amplitude drift between measurements. Note that because we do not have a simultaneous harmonic amplitude reference measurement, a change in the XUV input flux during this measurement can manifest itself as a change in the absorbance. A typical ground state measurement of a 100 nm Ge sample is shown in Fig. 1.12.

The transient data collection sequence can be summarized as *excited state*  $\rightarrow$  *ground state*  $\rightarrow$  *move motors*. Details of this sequence are as follows. First, the sample moves to a given raster position and delay wedge position, the IR shutter opens and an excited state spectrum  $S_{\text{sig}}(\tau, E)$  is recorded. Then, the IR shutter closes and a ground state spectrum  $S_{\text{gs}}(E)$  is recorded. To minimize the duration of the experiment, an XUV reference spectrum  $S_{\text{vac}}(E)$  is not recorded. Finally, the sample moves to the next raster position as the delay wedge pair moves to the next delay position. The system is programmed to wait for the wedges to become stationary before the next measurement begins.

Note that in this sequence, the time between the  $i^{\text{th}}$  excited state and  $i^{\text{th}}$  ground state measurements is equal to the exposure time, but the time between the  $i^{\text{th}}$  ground state measurement and the  $(i+1)^{\text{th}}$  excited state measurement is equal to the delay wedge motor

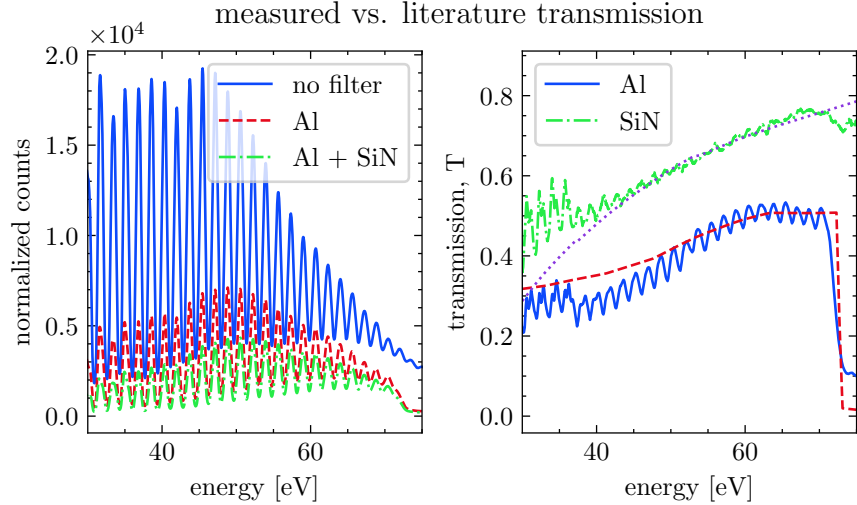


Figure 1.8: XUV transmission measurements of Al metallic filter and silicon nitride membrane. Left panel: normalized XUV counts for i) unfiltered HHG signal, ii) HHG going through a 200 nm Al filter and iii) HHG going through a 200 nm Al filter and 30 nm of silicon nitride. Counts are scaled by the Jacobian. Right panel: transmission curves obtained from the left panel's data. Also shown are literature values for 20 nm of silicon nitride and 200 nm of Al with two 4 nm oxide layers [6]. Multilayer interference is not taken into account. Oscillations in measured transmission are numerical artifacts which will be discussed in the text.

transit time<sup>2</sup>. This sequence is preferable to the alternative (*ground state*  $\rightarrow$  *excited state*  $\rightarrow$  *move motors*), as that would result in a delay step size-dependent relaxation time between the  $i^{th}$  excited state and the  $i+1^{th}$  ground state measurement. Since  $\Delta A(E, \tau)$  is calculated between pairs of ground and excited state measurements at a given delay wedge position, the sequence *excited state*  $\rightarrow$  *ground state*  $\rightarrow$  *move motors* is preferred.

To further improve our signal-to-noise ratio, we average multiple delay scans together. A typical  $\Delta A$  measurement will be repeated between 5 and 50 times. Each delay scan uses the raster points of the previous delay scan so there is a one-to-one mapping of delay to sample position.

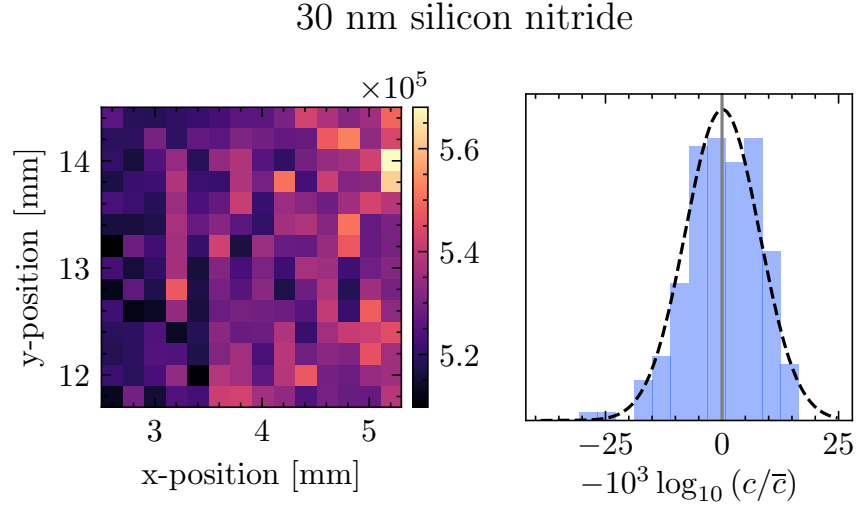


Figure 1.9: XUV transmission map of 30 nm silicone nitride freestanding membrane. Left panel: integrated XUV counts in the range 30 – 34 eV. Sample holder motor positions are indicated by x- and y-positions. Right panel: histogram of logarithmic deviation of counts from the average. Dashed line shows a normal distribution.

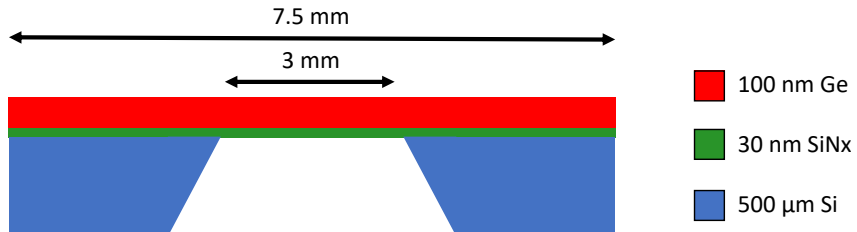


Figure 1.10: Cartoon showing the cross section of the free standing sample heterostructure. A 500  $\mu\text{m}$  thick Si frame supports a freestanding 30 nm low stress silicon nitride membrane (Norcada QX7300X), upon which 100 nm of germanium has been deposited. The Si frame has a 3x3  $\text{mm}^2$  square clear aperture and a 7.5x7.5  $\text{mm}^2$  square external dimension. The taper of the Si frame thickness along the perimeter of the clear aperture forms a knife edge. In an ATAS experiment, the XUV and IR pulses propagate from the top to bottom of the figure.

## 1.6 The Supporting Nitride Membrane

While most materials have an absorption edge within the range 25 - 150 eV, there are very few commercially available pre-fabricated materials with both the requisite large clear aperture and thickness. Note that either characteristic is relatively easy to achieve individually, but their combination presents unique materials challenges. We considered three synthesis methods to produce this quasi-2D sample:

1. sample growth on a traditional substrate, followed by chemical back-etching or milling of the substrate until sub-micron thickness of the heterostructure is achieved;
2. sample growth on a traditional substrate, followed by mechanical transfer onto a membrane;
3. sample growth on a membrane.

Sample quality and composition is heavily impacted by local growth conditions such as substrate temperature, deposition rate, substrate crystal cut, substrate-sample lattice mismatch, etc. Many of these characteristics are changed when growing on a substrate of a different cut, or by replacing a substrate with a membrane. In general, one should not expect success when applying a substrate-optimized growth recipe to a freestanding membrane. Therefore, methods 1 and 2 will yield the highest quality samples, as they leverage already-developed sample recipes. However, both methods require a technically difficult second step that is prone to failure.

Selective chemical etching recipes exist for certain compounds, but they usually require an additional chemically inert layer in the heterostructure to protect the sample. Adding this layer will come at the expense of the total XUV flux transmitted by the heterostructure. Additionally, the chemical etching rates are highly dependent on local chemistry, fluid convection and temperature [2], which ultimately means that the amount of material removed is uncontrollable and unrepeatable within our requirements ( $499.9 \mu\text{m} \pm 10 \text{ nm}$  removed

<sup>2</sup>In this analysis we neglect the role of the XUV-IR delay  $\tau$ . However,  $\tau \sim 1 \text{ fs} - 1 \text{ ps}$ , which is negligible compared to the motor transit time  $\sim 1 \text{ s}$ .

from a  $500 \mu\text{m}$  substrate). For these reasons, we decided to not pursue a chemical etch recipe. Ion or electron milling is more controllable, but too expensive to implement on a large scale. The above reasons preclude the use of Method 1.

Mechanical transfer of thin samples is a tried and true method, but it usually results in flakes with lateral dimensions on the order of  $100 \mu\text{m}$ . Repeated transfer of many flakes is possible, but there little control over their exact positioning on the membrane. This results in a random distribution of flakes; the flakes are sometimes folded or overlapping one another. These mishaps increase the effective optical density of the sample, changing the IR and XUV absorption properties significantly.

An XUV spatial measurement needs to be taken prior to any ATAS experiment, but a non-uniform distribution of flakes on a membrane would require a much higher resolution map. This is because the flakes are on the order of the XUV and IR focii, so it is critical that the raster points in Fig. 1.7 correspond to the center of each flake to avoid edge diffraction and to minimize the effects of slow laser pointing drift. For a uniform film, a map can be taken using  $200\text{-}250 \mu\text{m}$  step sizes, as the most important feature is the border of the clear aperture. On the other hand, each flake would have to be sampled  $\sim 5$  times in each direction to find its center. As a conservative estimate, a membrane covered with  $100 \times 100 \mu\text{m}^2$  flakes would require a step size of  $20 \mu\text{m}$ , which increases the number of raster points by a factor of  $10^2 = 100$ . Considering that a  $3 \times 3 \text{ mm}^2$  clear aperture sampled with  $200 \mu\text{m}$  steps takes  $\sim 45$  minutes to map, a random distribution of flakes would take a prohibitively long time to map out.

With the first two methods ruled out, we turn to the third method of growing directly on a freestanding membrane. Although it will result in a lower quality sample, it does not have the same technical hurdles of the previous two methods. However, the large clear area makes the heterostructure extremely fragile. We initially attempted to circumvent this problem by using an array of smaller clear apertures.

As shown in Fig. 1.7, most of the sample's area isn't directly used by the laser - it exists as a buffer between the grid of sample points. An alternative to a single clear aperture is an array of micro-apertures, each with a diameter on the order of the IR spot size. The micro-

apertures exist within a mechanically robust substrate and a thin membrane lies on top of the structure. This configuration significantly eases the material strength requirements by reducing the size of the unsupported area from cm-scale to sub-mm-scale. The regular grid of apertures avoids the difficulties of a randomly distributed sample, easing the XUV mapping step size requirements. Fortunately, these arrays are commercially available from Silson, Norcada (silicon nitride membranes) and US Applied Diamond (diamond membranes) but we encountered technical difficulties in their implementation. Because the aperture size is on the order of the size of the IR focal spot, there is very little room for positioning error, and our motors were insufficiently precise for this application. Further, these arrays are typically only available in at most a  $3 \times 3$  array, which provides an insufficient number of raster points for an ATAS experiment.

With these limitations in mind, we decided to use large aperture x-ray windows from Norcada. These windows consist of a mechanically robust Si frame substrate with a square clear aperture cut through the center. The structure is fabricated so that a thin membrane covers the clear aperture. A schematic of the cross section is shown in Fig. 1.10.

Norcada offers these structures with either a silicon (polycrystalline or single-crystal) or a silicon nitride membrane. An ideal membrane is transparent to both XUV and IR wavelengths with a high damage threshold. Referring to Fig. 1.5, 100 nm of Si provides a relatively flat transmission curve from 25 to 100 eV. In contrast, 30 nm of silicon nitride has poor, but featureless, transmission at lower energies. Both materials transmit light below their bandgaps (5 eV for SiN and 1.14 eV for Si). Finally, silicon nitride's higher bandgap results in a significantly higher laser damage threshold [1, 5, 9]. Taking all these factors into account, we decided to use 30 nm silicon nitride membranes for germanium transient absorption experiments. The measured transmission of a typical membrane is shown in Fig. 1.8.

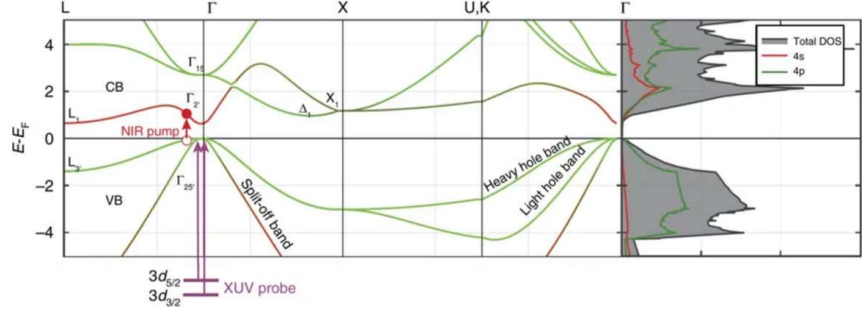


Figure 1.11: Band structure and orbital character of germanium. Purple arrows indicate XUV-induced transitions from the  $3d$  core levels to the valence bands. Red arrow indicates IR-induced transition across the direct band gap. Figure adapted from [15].

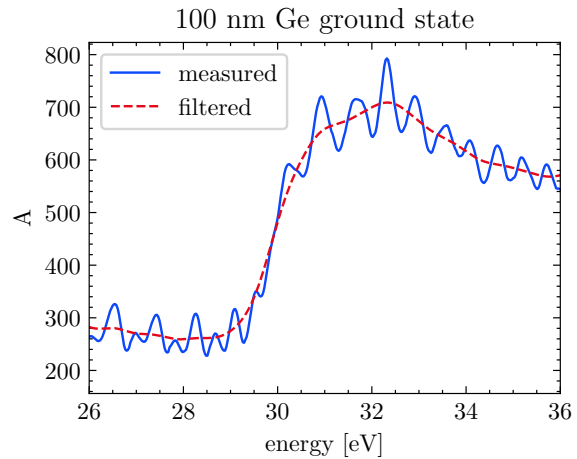


Figure 1.12: Measured ground absorbance  $A$  of a 100 nm Ge film on a 30 nm silicon nitride membrane. The contribution of the membrane has been subtracted. Blue line is the measured absorbance  $A$ . The red dashed line shows the result of numerical filtering to eliminate numerical artifacts (described in main text).

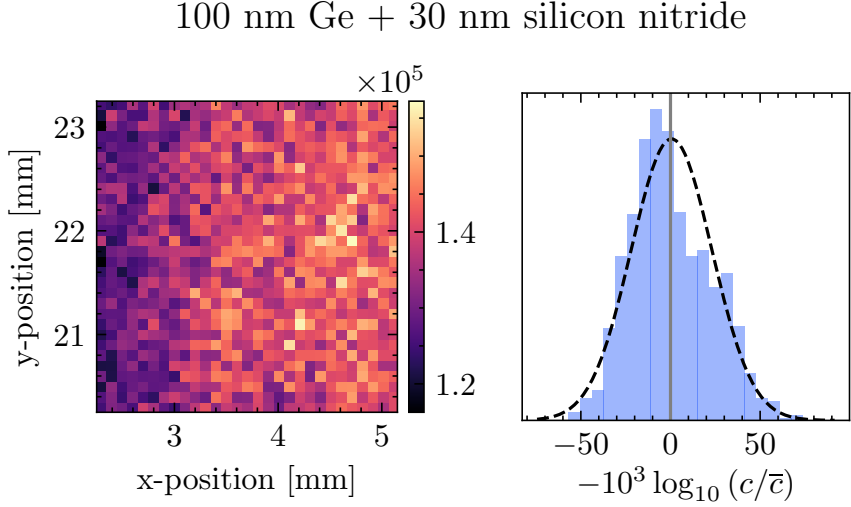


Figure 1.13: Left panel: spatial mapping of integrated XUV counts (30 – 34 eV) of a 100 nm Ge + 30 nm silicon nitride sample. Right panel: normalized histogram of counts  $c$  from the left panel.

## 1.7 The Germanium Sample

Germanium is a technologically important semiconductor with an indirect bandgap of 0.66 eV (1880 nm) and a direct gap of 0.8 eV (1550 nm). Its small band gap allows for single-photon excitation using the signal output of our TOPAS.

The band structure of Ge is shown in Fig. 1.11. DFT calculations [15] indicate that the valence band has primarily  $4p$  orbital character, and the conduction band has equal parts  $4s$  and  $4p$  character. However, the orbital character of the conduction band in the  $\Gamma$  valley is primarily  $4s$ .

The  $M_{4,5}$  absorption edge in germanium is near 30 eV, which corresponds to a transition between both the  $3d_{5/2}$  (-29.3 eV relative to the Fermi energy) and  $3d_{3/2}$  (-29.9 eV) states to the states near Fermi level. The ground state absorbance of germanium as measured with the TABLE apparatus is shown in Fig. 1.12. The  $M$  edge is easily visible in the measured data, with the absorbance more than doubling across the edge.

The transition  $3d \rightarrow 4s$  is forbidden from the dipole selection rules, but  $3d \rightarrow 4p$  is allowed. Therefore, the XUV primarily probes the valence band in the  $\Gamma$  valley. This

is depicted in Fig. 1.12 as purple arrows. IR light with a photon energy exceeding the bandgap will promote electrons across the direct bandgap, which is indicated as a red arrow in Fig. 1.12, leaving behind a hole in the valence band.

Germanium is a good sample for a number of reasons. First, it has an XUV absorption feature at a relatively low photon energy, where we have bright XUV flux. We are able to tune our generation conditions to optimize this part of the XUV spectrum while simultaneously suppressing the generation of photons at higher energies which can artificially distort the measured spectrum. Second, we can access the bandgap using the signal output of our TOPAS. Finally, its simple chemistry means that samples can be grown in quantity using simple electron beam deposition techniques.

Ultrafast dynamics in germanium have previously been studied using few-cycle VIS-NIR light ( $\lambda = 800$  nm) in both transmission [15, 16] and reflection geometries [8]. However, the ultrafast dynamics of this material have not been studied using longer wavelength excitation than our lab is capable of creating. To this end, approximately 100 nm of germanium was deposited onto a 30 nm silicon nitride membrane using electron beam deposition (Kurt J. Lesker Lab 18) in the NanoSystem's Laboratory. A typical XUV map of a Ge sample on a nitride membrane is shown in Fig. 1.13.

## 1.8 IR Pump Arm Considerations

In a condensed matter ATAS measurement, the IR intensity is usually set to be as high as possible (while avoiding sample damage) to maximize the sample's transient response. Under these conditions,  $\sim 1\%$  of valence electrons are excited across the bandgap by the laser [4, 12, 15]. Calculations were performed to estimate the input laser power necessary to achieve the appropriate excitation fraction, but ultimately the input power needs to be determined experimentally through trial and error. Note that many of these calculations are linear with respect to input pulse energy, so we use a  $1 \mu\text{J}$  pulse to make the final result easily scalable.

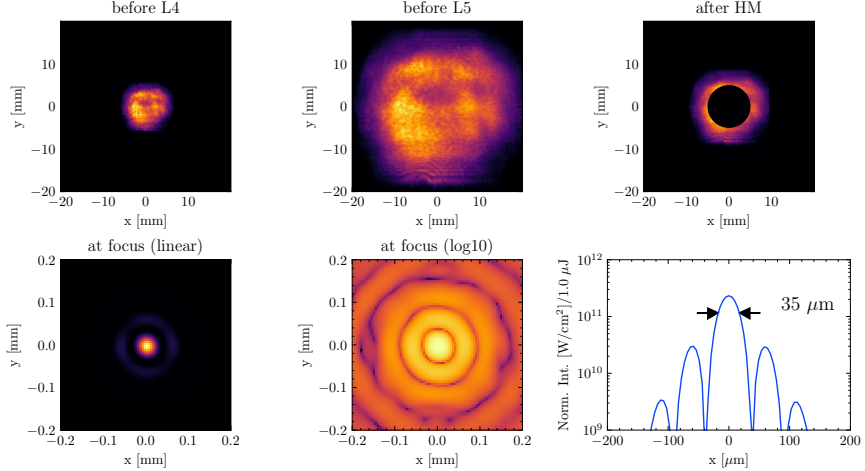


Figure 1.14: Numerical propagation of the IR ( $\lambda=1500$  nm) beam through the pump arm. Beam path layout follows Fig. 1.1. Each panel shows the intensity of the beam as the beam propagates towards the focus. The first panel shows the measured intensity (Electrophysics PV320 thermal camera), all other panels are calculations. The arrows on the lineout indicate the FWHM. All calculations are for vacuum ( $n = 1$ ). See text for details.

### 1.8.1 Calculation of IR Intensity at Focus

The profile of the TOPAS output at  $\lambda=1500$  nm was measured immediately before the pump arm's diverging lens (L4 in Fig. 1.1) using an Electrophysics PV320 thermal camera. The beam was propagated numerically using the Python package *Lightpipes for Python* [13] through the remainder of the pump arm to the focus using a grid size of  $2^{13} \times 2^{13}$ . The result of this calculation is shown in Fig. 1.14. Optical element parameters are as follows: L5 is a  $f = +500$  mm Thorlabs LA1380-C, located 68.5 cm after L4 ( $f = -300$  mm, Thorlabs LF1015-C). The hole mirror HM is located 53 cm after L5 and has an inner radius of 5 mm. Clear apertures of 22.86 mm (L4), 45.72 mm (L5) and 50.8 mm (HM) were used. A 65 fs Gaussian temporal profile containing 1  $\mu\text{J}$  of energy was assumed.

Reflection losses from 2 Ag mirrors, 2 AR-coated lenses and uncoated CaF<sub>2</sub> vacuum window are responsible for a 26.2% reduction in transmitted power. Additionally, the geometry of the hole mirror causes only 56% of incident power to be incident on a reflective surface (the rest is lost to the central aperture). In total, the pump arm transmits 41.3% of the power from before L4 to the focus.

The IR intensity makes an Airy-like diffraction pattern at the focal plane. There is an intense bright spot surrounded by a series of rings, with the intensity of each ring as the distance from the center increases. The rings exhibit a periodic modulation in intensity with respect to angle  $\phi$ . This four-fold symmetry is due to the square-like spatial profile of the TOPAS output, whereas the clipping from the hole mirror's aperture is responsible for the central peak and ring structure. The central lobe has a peak intensity of  $\sim 2.3 \times 10^{11} \text{ W/cm}^2$  per  $1 \mu\text{J}$  input pulse energy and a FWHM of  $35 \mu\text{m}$ . The first ring has a radius of  $59 \mu\text{m}$  and a peak intensity  $\sim 2.9 \times 10^{10} \text{ W/cm}^2$  per input  $\mu\text{J}$  pulse energy. Thus the central lobe's peak intensity is about an order of magnitude larger than the ring's intensity. However, the central spot only contains about 49% of the total power, as the rings cover a much larger area.

Note that the above calculations assume perfect alignment into the hole mirror (i.e., the IR beam is centered on the central aperture of the hole mirror). If the IR beam is misaligned to the hole mirror, then the transmission to the focus will increase as the most intense part of the beam is no longer clipped by the central aperture. Therefore, a drift in the laser's pointing during an experiment can effect the sample's interaction intensity.

### 1.8.2 Estimation of Excited Carrier Density

We are concerned with two quantities: the peak excitation fraction in the sample and the average excitation fraction at the location of the XUV focus. The former quantity is relevant when considering sample damage, whereas the latter will be proportional to the measured signal. If the XUV and IR spots are perfectly overlapped at the sample plane, then these two quantities are approximately equal. We first calculate the peak excitation fraction, then we consider how a misaligned beam will affect the measured signal.

The laser propagation calculations in Fig. 1.14 were done for vacuum, but we are concerned with the field in our sample. The electric field inside a dielectric  $E_{\text{int}}$  is related to the external electric field by the following equation [12]:

$$E_{\text{int}} = \frac{2}{1 + \sqrt{\epsilon}} E_{\text{ext}} \quad (1.13)$$

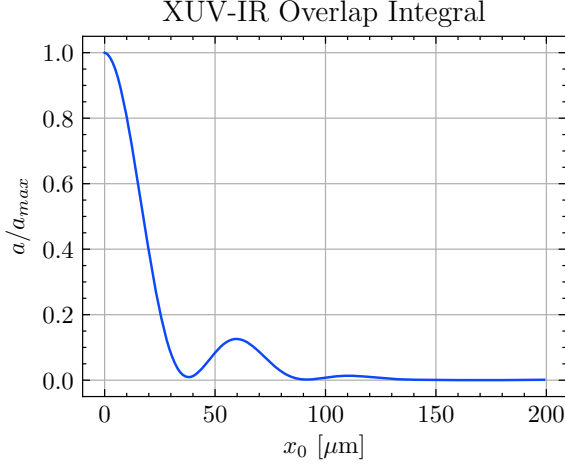


Figure 1.15: XUV-IR overlap function, as defined in Eq. (1.19), calculated using the numerical simulation results of Fig. 1.14 and a Gaussian XUV beam with a 6  $\mu\text{m}$  waist. The result has been normalized to perfect overlap,  $a_{max}$ .

where  $E_{int}$  is the electric field inside the sample,  $E_{ext}$  is the electric field outside the sample,  $\epsilon$  is the dielectric constant and its square root is the refractive index  $n_{IR}$ . The internal intensity  $I_{int}$  is the square of the internal electric field. For germanium at  $\lambda = 1430$  nm,  $n_{IR} = 4.2481$ , and we have the following relations:

$$\begin{aligned} E_{int} &= 0.381 \times E_{ext} \\ I_{int} &= 0.145 \times I_{ext} \end{aligned} \tag{1.14}$$

Given our laser parameters, we can estimate the highest carrier density within the sample. First, we estimate the absorbed laser fluence,  $F_{abs}$  [7]:

$$F_{abs} = F_{inc} (1 - R) (1 - \exp(-\alpha L)) (1 + R \exp(-\alpha L)), \tag{1.15}$$

where  $F_{inc}$  is the incident fluence,  $R$  is the reflectivity equal to the square of the Fresnel coefficient,  $\alpha$  is the absorption coefficient and  $L$  is the sample thickness. The bracketed terms in Eq. (1.15) are the fraction of fluence transmitted by the first surface, the fraction absorbed by a single pass through the sample, and the additional absorption due to a back reflection off the rear face of the sample. Note that the back-propagating beam will arrive (on average) at a delay of  $n_{IR}L/(2c) \approx 0.7$  fs later than the forward-propagating beam.

This time scale is nearly two order of magnitude less than the IR pulse duration, so we should expect any electron dynamics initiated by the back reflection to contribute to the measured signal.

If each absorbed photon corresponds to an excited electron, then the excited carrier density  $\Delta N$  is given by the following expression [4]:

$$\Delta N = \frac{F_{\text{abs}}}{\hbar\omega} \frac{1}{L}, \quad (1.16)$$

where  $\hbar\omega$  is the IR photon energy. In Eq. (1.16), the quantity  $F_{\text{abs}}/(\hbar\omega)$  represents the number of absorbed photons per unit area; dividing this quantity by the sample thickness gives the number of absorbed photons per unit volume. This assumes that the skin depth of the material is greater than membrane thickness, which is true for germanium at these wavelengths.

Finally, we convert the excited carrier density to a fractional excitation. Germanium has  $N_{\text{u.c.}} = 2$  valence electrons per unit cell, and each unit cell has a volume  $V_{\text{u.c.}} = 4.527 \times 10^{-23} \text{ cm}^3$ . Therefore the fractional carrier excitation is

$$f = \Delta N \frac{V_{\text{u.c.}}}{N_{\text{u.c.}}} \quad (1.17)$$

We can use literature values for 100 nm of germanium pumped at  $\lambda = 1430$  nm light. From the literature [11],  $R = 0.38315$ ,  $\alpha = 5803.4 \text{ cm}^{-1}$ , and so  $F_{\text{abs}} = 0.0413 \times F_{\text{inc}}$ . Therefore, only about 4.13% of the incident fluence is absorbed by the sample.

According to the calculations in Fig. 1.14, for each 1  $\mu\text{J}$  energy input pulse (measured at L4), 0.413  $\mu\text{J}$  makes it to the focal plane. 49% of that energy is within the main lobe, which contains 0.202  $\mu\text{J}$  of energy. Approximating the central lobe as a Gaussian beam with a FWHM of 35  $\mu\text{m}$  and a pulse energy of 0.202  $\mu\text{J}$ , the peak fluence is calculated by dividing the total energy of the Gaussian by  $\pi w^2/2$ . The Gaussian beam waist  $w$  is related to the FWHM via  $w^2 = \text{FWHM}^2/(2 \ln 2)$ . Thus, for each 1  $\mu\text{J}$  input energy, the peak fluence in the central lobe is 14.6  $\text{mJ}/\text{cm}^2$  and the absorbed peak fluence is 0.60  $\text{mJ}/\text{cm}^2$ . This corresponds to an peak excited carrier density of  $4.3 \times 10^{20} \text{ cm}^{-3}$  and an excitation fraction of 0.98% (per 1  $\mu\text{J}$  of input energy).

### 1.8.3 The XUV-IR Overlap Integral

The excitation fraction can be computed for each spatial coordinate on the sample using the above method and the predicted intensity distribution from the numerical beam propagation calculations. Because the electrons are being excited via a single-photon process, the excited carrier density will be proportional to the fluence, and thus proportional to the intensity shown in Fig. 1.14. Because the intensity of the XUV is very weak, the absorption of the XUV by the sample is also linear. Thus, we should expect the ATAS signal to be proportional to the XUV-IR overlap integral:

$$a = \frac{\int dV I_{\text{IR}} I_{\text{XUV}}}{\int dV I_{\text{IR}} \int dV I_{\text{XUV}}} \quad (1.18)$$

Here, the integration volume is over the entire sample. If we assume that the intensity distribution does not appreciably change over the thickness of the sample, we can simplify the above equation. This is a reasonable assumption because the sample ( $L = 100$  nm) is much thinner than the Rayleigh range ( $z_R \sim 1$  mm), and the absorption is low ( $\sim 4\%$ ). So we assume the sample is a  $\delta$ -function in thickness and only evaluate the intensities at the focal plane. With this assumption, the overlap integral becomes:

$$a = L \frac{\int dA I_{\text{IR}} I_{\text{XUV}}}{\int dA I_{\text{IR}} \int dA I_{\text{XUV}}} \quad (1.19)$$

Knife edge measurements have been performed on the XUV light, showing that it has a Gaussian spatial profile with a beam waist of  $6 \mu\text{m}$ . We write down the spatial profile of the XUV light at the focus:

$$I^{\text{XUV}} = I_0^{\text{XUV}} \exp(-2((x - x_0)^2 + (y - y_0)^2)/w_{\text{XUV}}^2) \quad (1.20)$$

Here,  $I_0^{\text{XUV}}$  is the peak intensity and  $w_{\text{XUV}}$  is the beam waist (radius), defined as the point where the intensity falls to  $e^{-2} = 13.5\%$  of its maximum. The lateral shift from the center of the IR focal spot in the horizontal and vertical directions is  $x_0$  and  $y_0$ , respectively. With this formulation, and using the simulation results for the IR spot, the XUV-IR overlap integral is calculated as a function of XUV-IR misalignment ( $x_0, y_0$ ). This result is shown in

Fig. 1.15. Here, XUV beam is translated relative to the IR beam in the horizontal direction ( $x_0$  with  $y_0 = 0$ ) and the overlap is computed from Eq. (1.19).

Fig. 1.15 shows the sensitivity of a condensed matter ATAS experiment to relative alignment.<sup>3</sup> A spatial overlap deviation of  $10 \mu\text{m}$  will cause the XUV-IR overlap - and thus the measured signal - to drop by 20%. Note that a  $10 \mu\text{m}$  displacement of the IR at the sample corresponds to a  $15 \mu\text{rad}$  tilting of the hole mirror (HM). There are two ways misalignment can affect experimental results. If the relative positions of the XUV and IR focal spots changes as an experiment is performed, then the recorded ATAS signal would be a function of both the laser-induced dynamics and the XUV-IR spatial misalignment. On the other hand, if the entire experiment is performed using a constant misalignment, we would be exciting the sample to some peak excitation fraction  $f$ , but our probe would be measuring a lower excitation fraction ( $\approx fa/a_{max}$ ). Consequently, the measured ATAS signal would be lower than otherwise expected, and any attempts to boost the signal by increasing the interaction intensity could result in permanent laser-induced sample damage.

A condensed matter ATAS experiment has much tighter alignment tolerances than a gas phase experiment. This discrepancy is a simple consequence of sample geometry and density. In either experiment, the measured signal comes from the region of space where the sample density, XUV intensity and IR intensity overlap. The transmission of XUV through the sample is, to first order,  $T = \exp(-n\mu_a d)$ , where  $n$  is the number density,  $d$  is the sample thickness and  $\mu_a$  is the photoabsorption cross section. As discussed above, for technical reasons the experiment should be designed with  $T \approx 1/2$ . Therefore, the product  $n\mu_a d$  will be approximately constant for any transient absorption experiment.

The number density of a condensed phase sample is determined by the chemistry of the compound and is on the order of  $4 \times 10^{22} \text{ atoms/cm}^3$ . The experimentalist is free to engineer clever sample geometries, heterostructures and/or nanopatterns, but the high atomic density (and thus absorption coefficient) dictates a total sample thickness on the order of 100 nm. On the other hand, the spatial profile and density of a gas phase sample

<sup>3</sup>Note that the relevant parameter in Eq. (1.19) is the relative positions of the two focal spots. We have yet to calculate the sensitivity of spatial overlap to deviations in the input laser pointing.

is determined by the gas nozzle design and its backing pressure, respectively. A typical nozzle used in our lab produces a gas plume with lateral dimensions on the order of 200 - 500  $\mu\text{m}$ . This effectively creates a sample that is three orders of magnitude thicker than a condensed phase sample, which relaxes the alignment constraints significantly. This has important consequences for the alignment of the sample.

If the XUV and IR are perfectly collinear, then the beam overlap region is effectively infinite in the propagation direction. In this case, the XUV-IR overlap integral will be positive regardless of any displacement of the sample plane from the focal plane, and maximal when the sample lies in the focal plane. However, if there is a small angle  $\delta\theta$  between their  $k$ -vectors, then the beams will only spatially overlap within a finite region. In this case, the position of the sample plane relative to the beam crossing plane becomes a critical experimental parameter. For an infinitely thick sample (i.e., a chamber effusively filled with gas), it wouldn't matter where the beams crossed as long as they overlapped somewhere within the chamber. Then, the overlap integral would decrease as a function of  $\delta\theta$ , but it would never go to zero. For a thin sample, the bounds of Eq. (1.18) must enclose the beam overlap region, or else the integral will be zero. Thus, the signal strength of a condensed phase ATAS experiment is roughly 3 orders of magnitude more sensitive to the  $z$ -position of the sample relative to the focal plane than a gas phase ATAS experiment.

## 1.9 Experimental Methods

In this section, the methods to find spatial and temporal overlap of the XUV and IR focal spots are discussed. Also detailed are the experimental methods for optimizing the pump arm and generation conditions for a condensed matter sample.

### 1.9.1 Finding XUV-IR spatial overlap

XUV is ionizing radiation and cannot propagate in air. However, due to macroscopic phase matching conditions, the XUV propagates in the same direction as the IR light that created it. Consequently, the XUV-IR spatial overlap can be achieved by aligning the IR beams

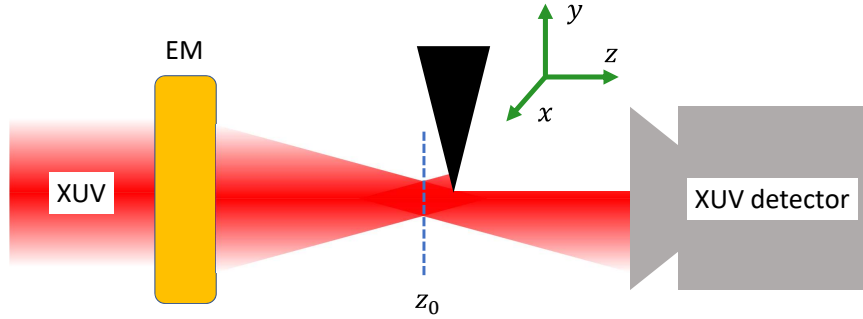


Figure 1.16: Schematic of XUV knife edge measurement. EM: ellipsoidal mirror,  $z_0$ : XUV focal plane.

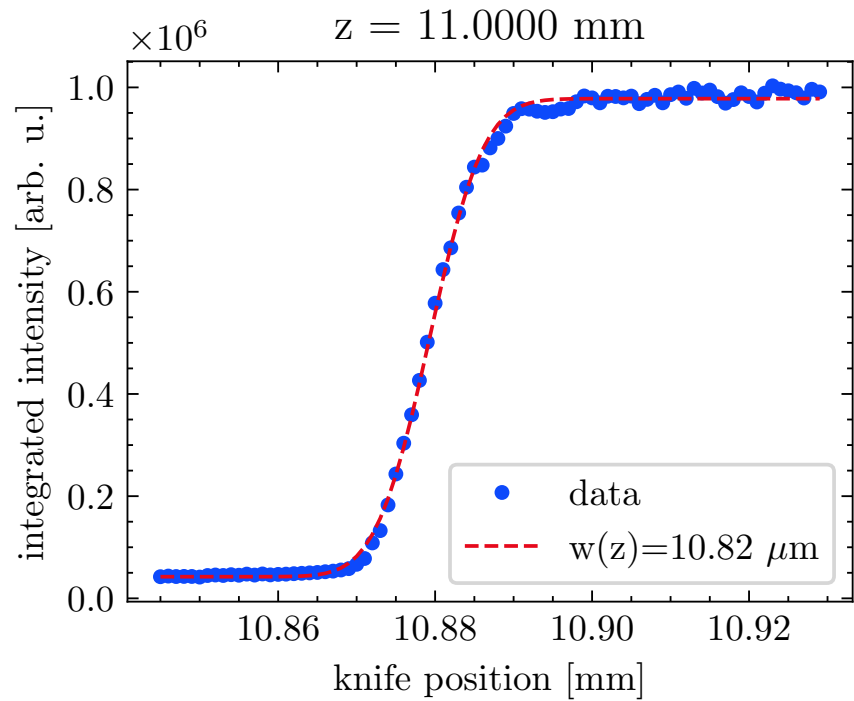


Figure 1.17: A typical XUV knife edge measurement near the focal plane. The sample motor position is  $k = 11.0000$  mm. A fit to equation Eq. (1.23) yields a beam waist of  $10.82 \mu\text{m}$  at this position.

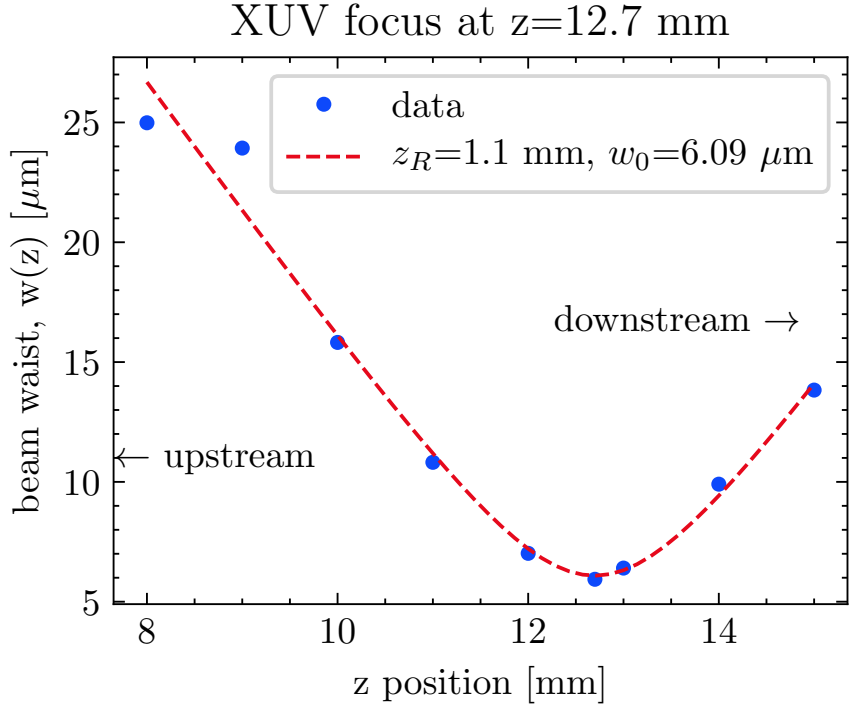


Figure 1.18: Evolution of XUV beam waist as a function of propagation direction,  $z$ . The Rayleigh range  $z_R$  and beam waist  $w_0$  are extracted from the fit to Eq. (1.22).

from both arms of the interferometer when the vacuum system is vented. This alignment is performed as follows.

First, we verify that the laser is pointing correctly into the interferometer using our fiducials.<sup>4</sup> We remove the sample holder from the target chamber and the metallic filter from the generation arm. This allows the generation arm's IR light to propagate downstream to the target chamber. We then place a pair of reflective and absorptive neutral density filters (OD = 7), a 1  $\mu\text{m}$  low-pass filter (Thorlabs FELH1000) and a digital camera (ImagingSource DMK 27AUJ003) in the target chamber so the sensor is at the focus of the generation arm's IR light. These temporary optics are common to both arms, so they do not change the relative position of the foci. Because the EM a reflective focusing optic and the intensity near the focus is low, the IR should focus to roughly the same position as the XUV light. We close an iris before L3 to limit the intensity and note the position of the centroid of

<sup>4</sup>Details of this process will be explained elsewhere.

the focus on the camera's sensor. The generation shutter is closed and this process is repeated for the pump arm, with the power being controlled by the  $\lambda/2$  waveplate-polarizer optics. The optical mount for the hole mirror has two vacuum compatible motors (Thorlabs Picomotors), which allow us to remotely change the two angles of this optic. By actuating these motors, we can control the lateral position of the pump arm's focus relative to the ellipsoidal mirror's focus. This process is iteratively repeated until the two foci are at the same location on the camera's sensor.

Due to phase matching, the optimal position of the high harmonic gas source is slightly downstream of the IR's focal position. As a result, the XUV will focus slightly upstream compared to the generation arm's IR that we used in the aforementioned alignment procedure. The exact distance between the gas cell and the IR focus depends on many factors, but it is on the few-millimeter scale. The ellipsoidal mirror has a 3:1 demagnification ratio, so for every 1 mm on-axis deviation in the generation chamber, we will have a  $1/3^2 = 1/9$  mm on-axis deviation in the target chamber. A correction of this size is within the limit of our target chamber sample motors, but it must be done in vacuum using XUV light.

To this end, we must generate the XUV light that will be used for the upcoming experiment. With the chambers still vented, we verify temporal overlap (described below) and reinstall the sample holder. Finally, the chambers are pumped down and the generation conditions are adjusted to optimize the harmonic flux.

We characterize the XUV focus in the target chamber by performing knife edge measurements at different  $k$ -positions, as depicted in Fig. 1.16. We use the interior angled edge of the Si frame on a broken sample heterostructure as a knife edge (see Fig. 1.10). This frame makes an excellent knife edge as it has a very well-defined geometry and fits in the sample holder. Recalling Gaussian optics, the assumed profile of the XUV beam is:

$$I(x, y, z) = I_0 \left( \frac{w_0}{w(z)} \right)^2 \exp \left( -2((x - x_0)^2 + (y - y_0)^2)/w(z)^2 \right), \quad (1.21)$$

using the coordinate system defined in Fig. 1.16. The XUV focus is at position  $(x_0, y_0, z_0)$ .

The beam waist  $w(z)$  will evolve as:

$$w(z) = w_0 \sqrt{1 + \left(\frac{z - z_0}{z_R}\right)^2}, \quad (1.22)$$

where  $z_R$  is the Rayleigh range. If we use the knife edge to block the transmission as depicted in Fig. 1.16, then the transmitted power will be:

$$P(x, z) = P_0 + \frac{P_{max}}{2} \left( 1 - \text{erf} \left( \frac{\sqrt{2}(x - x_0)}{w(z)} \right) \right), \quad (1.23)$$

where  $x$  is the insertion of the knife in the beam,  $z$  represents the location of the knife plane in the propagation direction, and erf is the error function.

A typical knife edge measurement is shown Fig. 1.17. In this measurement, the knife edge is translated across the XUV spot in  $1 \mu\text{m}$  steps until the XUV light is completely blocked. A 2D spectrum is saved at each knife edge position. Each image is background subtracted, normalized and summed (integrating over all divergences and wavelengths), which yields the XUV flux as a function of knife position. The resulting curve is fit to Eq. (1.23) and the beam waist  $w(z)$  is extracted for this  $z$ -position.

The knife edge measurement is repeated at different  $z$ -positions until enough data has been acquired to determine the focal plane. The evolution of the XUV beam waist is shown in Fig. 1.18. In this figure, the beam waist has been fit to Eq. (1.22) to determine the focal plane  $z_0$ , the Rayleigh range  $z_R$  and the beam waist  $w_0$ . In both figures, a reasonably good fit is obtained, indicating that the XUV light has a Gaussian spatial profile near the focus.

It must be verified that the pump arm's IR light focuses to the same focal plane as the XUV. Therefore, the chambers are vented a second time, the sample holder removed, and the digital camera optics and filters installed. The k-position of pump arm's focus is moved up/downstream by moving L4, which is mounted on a translation stage.<sup>5</sup>

<sup>5</sup>The focusing optics in the pump arm are slightly chromatic, so L4 must be adjusted if the wavelength is changed.

### 1.9.2 Finding XUV-IR Temporal Overlap

Temporal overlap can be found under vacuum or in air. In either case, spatial alignment must already be achieved. If the chambers are vented, temporal overlap can be checked using a camera at the focus to observe interference fringes. Note that the presence of air in the generation arm introduces an additional path length of  $\approx (3 \text{ m}) \times (n - 1) \approx 820 \mu\text{m}$ . Therefore, the pump arm needs to be shortened by moving the retro reflector approximately  $(3 \text{ m}) \times (n - 1)/(2n) \approx 410 \mu\text{m}$  to recover overlap when the system is under vacuum.

Overlap can be found under vacuum by routing the collinear IR beams outside of the chamber after the focus. A translatable silver mirror, controlled by a set of gears and a linear shift vacuum feedthrough, is used to direct the light through a viewport on the spectrometer chamber wall. The light is focused by a  $f = +750 \text{ mm}$  lens (Thorlabs LA1727-C) onto a camera. Note that the spatial profile of the IR beam is not preserved during this routing, as the beam is heavily clipped by a vacuum aperture that separates the target chamber from the spectrometer. As a result, this method *cannot* be used to confirm spatial alignment of the foci. However, enough light makes it through to view interference fringes at overlap.

A BBO crystal, installed in one of the sample holder's sample slots in the target chamber, can also be used to find overlap. The intensity in each arm should be set so that SHG is produced only at temporal and spatial overlap.

### 1.9.3 Optimization of IR Pump Parameters

The arguments in Section 1.8.2 provide a starting point for the interaction intensity, but the optimum excitation intensity must be determined experimentally by observing how the sample response scales with interaction intensity. Unlike a gas phase sample a condensed phase sample can suffer permanent laser-induced damage, which complicates any intensity investigation. The exact damage mechanism was not studied but we have observed two modes of membrane failure, as shown in Fig. 1.20. Occassionally, the volume near the IR focal spot will be ablated by the laser, leaving the rest of the sample undamaged. The most common failure mode results in the immediate destruction of the entire sample, often

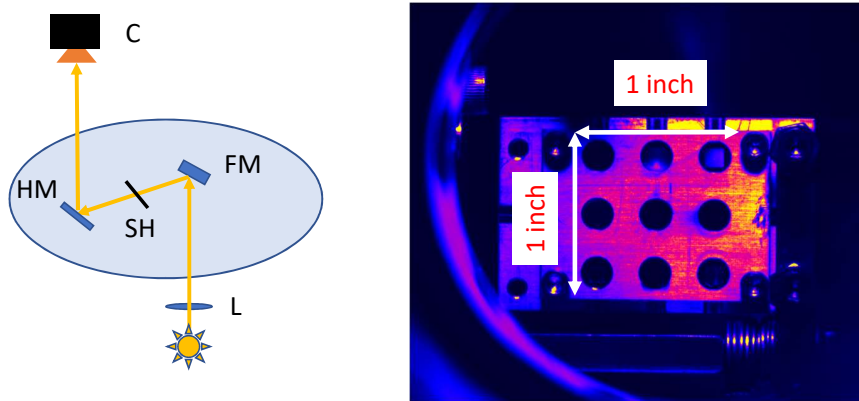


Figure 1.19: *In-situ* imaging of the samples within the target chamber. Left: optical setup for *in-situ* imaging of samples. C: Si CCD camera, HM: hole mirror, SH: sample holder, FM: translatable silver mirror, L: lens. Right: false color image showing the sample holder with a 3 x 3 grid of 5 mm diameter clear apertures. Samples are held in a clamshell design centered in the clear apertures and are backlit using a flashlight.

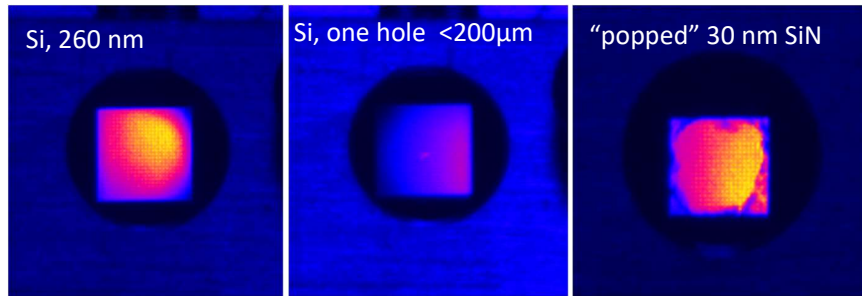


Figure 1.20: False color images showing laser drilled freestanding membranes. Left: pristine 260 nm thick Si membrane (Norcada). Middle: same sample, after performing an IR power scan that exceeded the membrane's damage threshold. A  $<200 \mu\text{m}$  hole is visible as a cluster of bright pixels near the center of the membrane. Right: 30 nm SiN membrane after a similar power scan showing a "popped" membrane. The ragged edges near the clear aperture of the frame are all that remain of the membrane. For all images, the apparent brightness gradient across the samples is caused by inconsistent backlighting. Images were taken using the optical setup shown in the left panel of Fig. 1.19.

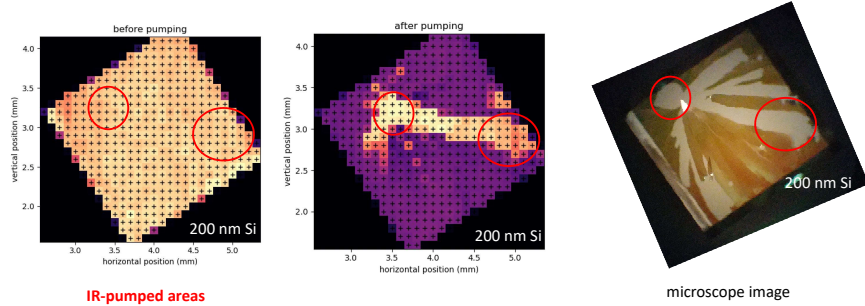


Figure 1.21: Laser damaged 200 nm silicon membrane samples. Left panel: XUV map of pristine Si before being exposed to IR laser. Higher transmission is indicated by brighter colors. Sample is rotated approximately 30 degrees relative to motor axes. Center panel: XUV map of damaged sample after being pumped with  $\approx 65 \mu\text{J}$  of  $\lambda = 1500 \text{ nm}$  at 1 kHz rep. rate in two locations. Damage occurred within the first camera exposure (2 seconds) and propagated to regions that were not exposed to the laser. Right panel: microscope image of damaged sample (beige) showing large sections of missing material (white). Red circles in all three pictures indicate the two locations that were exposed to IR laser light.

within a single camera exposure. Sample damage is apparent in both the visible and the XUV, as shown in Fig. 1.21.

The IR intensity incident on the sample is controlled by a motorized achromatic  $\lambda/2$  waveplate (Thorlabs AHWP10M-1600,  $\lambda = 1100 - 2000 \text{ nm}$ ) and a pair of ultra broadband wire grid polarizers (Thorlabs WB25M-UB, each with a 1000:1 extinction ratio for  $\lambda = 0.6 - 4 \mu\text{m}$ ) in the pump arm (see Fig. 1.1). A  $1 \mu\text{m}$  longpass filter (Thorlabs FELH1000, OD > 5) is positioned before the waveplate-polarizer assembly to filter out the OPA's visible parasitic wavelengths. During an experiment, the intensity is measured using an InGaAs photodiode (Thorlabs DET10D) mounted with a 2.0 absorptive neutral density filter and 1  $\mu\text{m}$  longpass filter (Thorlabs FELH1000), which detects light scattered off a mirror in the pump arm and is monitored using an oscilloscope (LeCroy). Absolute measurements of the average IR power were taken with a power meter (Gentek) located before the diverging lens L4.

As will be described below, the existence of long lived excited states further inhibits the study of ultrafast processes. To this end, ATAS experiments were performed to find the optimal rep. rate, pulse energy and wavelength.

## Feature Scaling with Rep. Rate

We performed exploratory experiments at 1 kHz to determine the optimal excitation pulse energy. For this set of measurements, we generated harmonics in Argon using  $\lambda = 1450$  nm, a 200 nm Al filter and the 2C optics removed (see Fig. 1.1). Two delay points were recorded: with the XUV and IR pulses overlapped ( $\tau = 0$ ) and with the XUV pulse arriving about 300 fs before the IR ( $\tau = -\infty$ ). For each delay point, we used three pulse energies: 1.03, 1.43 and 1.75  $\mu$ J. To increase the signal-to-noise, we performed each experiment 104 times and averaged the datasets. The exposure time was 0.5 seconds, and the sample was rastered so that each measurement was recorded at a new position on the sample. The results are shown Figs. 1.22, 1.23a and 1.23b.

Figs. 1.22a to 1.22d and 1.23a show the average  $\Delta A$  as a function of the number of averaged measurements,  $M$ . Spectral features are apparent after averaging about 10 datasets together, but the fidelity of the signal does not appreciably improve after the first  $M = 50$  datasets. Figs. 1.22e and 1.22f show the average signal (lines) and the standard deviation (shaded area), as calculated from the entire ensemble of measurements. The data is noisy, but we can see a spectral feature near 30 eV which scales with pulse energy (or perhaps average power). This behavior is evident in Fig. 1.23b. However, this feature is delay-independent:  $\Delta A$  has nearly the same value regardless of whether the XUV arrives before or after the IR pulse.

To confirm the delay-independence of this feature, we performed delay scans at two different pulse energies (1.43 and 1.75  $\mu$ J). These measurements are shown in Fig. 1.23. Delay was controlled by inserting a fused silica wedge into the interferometer (W in Fig. 1.1). Each delay step corresponds to approximately 3.25 fs (25  $\mu$ m of wedge insertion).

The raw data is shown in Figs. 1.23c and 1.23d. As this experiment was only performed once ( $M = 1$ ), the contrast is poor and the 30 eV feature is barely visible. The spectral feature becomes more prominent after performing a rolling average over 20 delay points (65 fs), which is shown in Figs. 1.23e and 1.23f. These delay measurements confirm our suspicion that the absorption feature is delay-independent at 1 kHz.

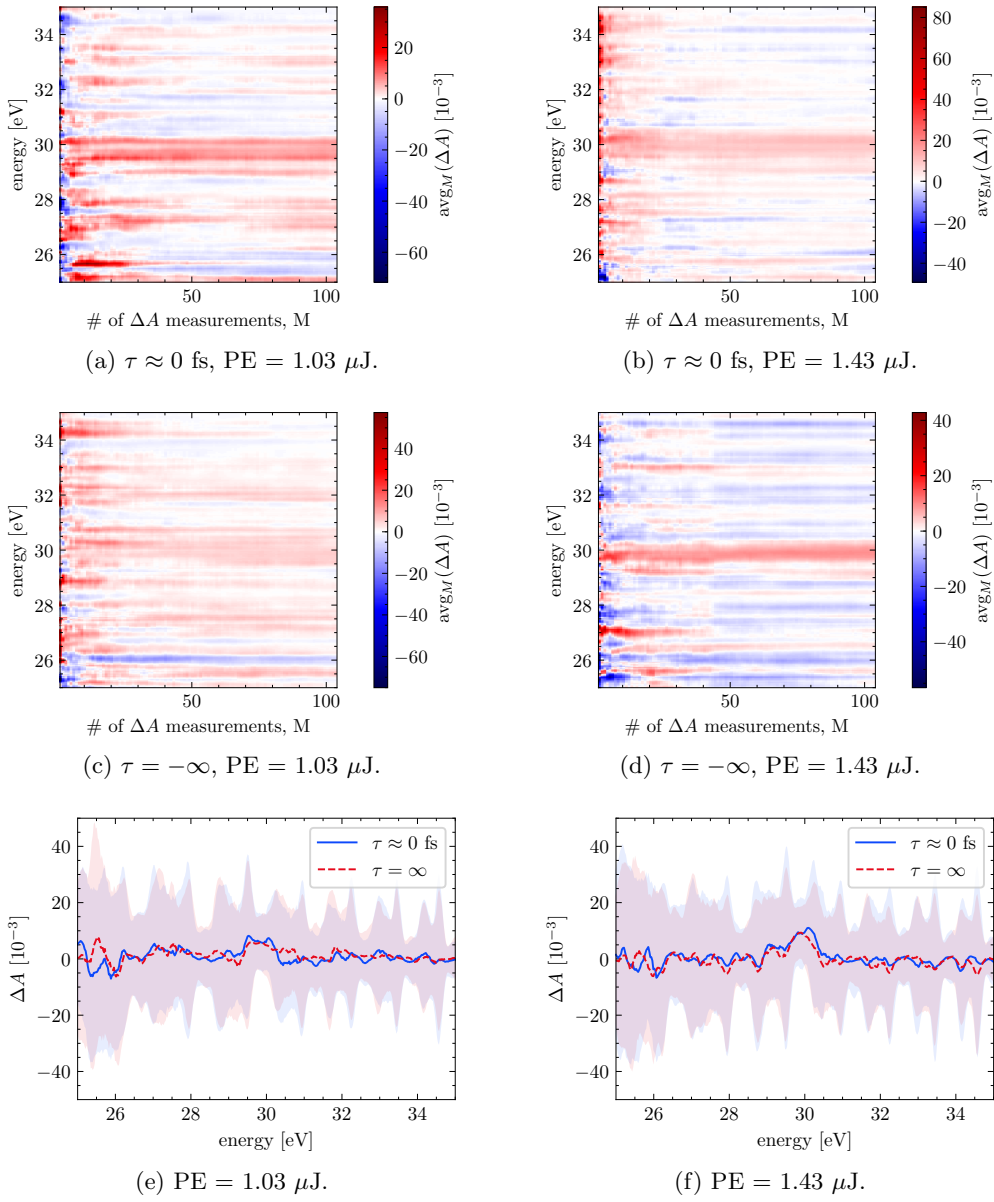


Figure 1.22: 1 kHz fixed-delay ATAS measurements on 100 nm Ge using a  $\lambda = 1450$  nm excitation pulse. See text for details.

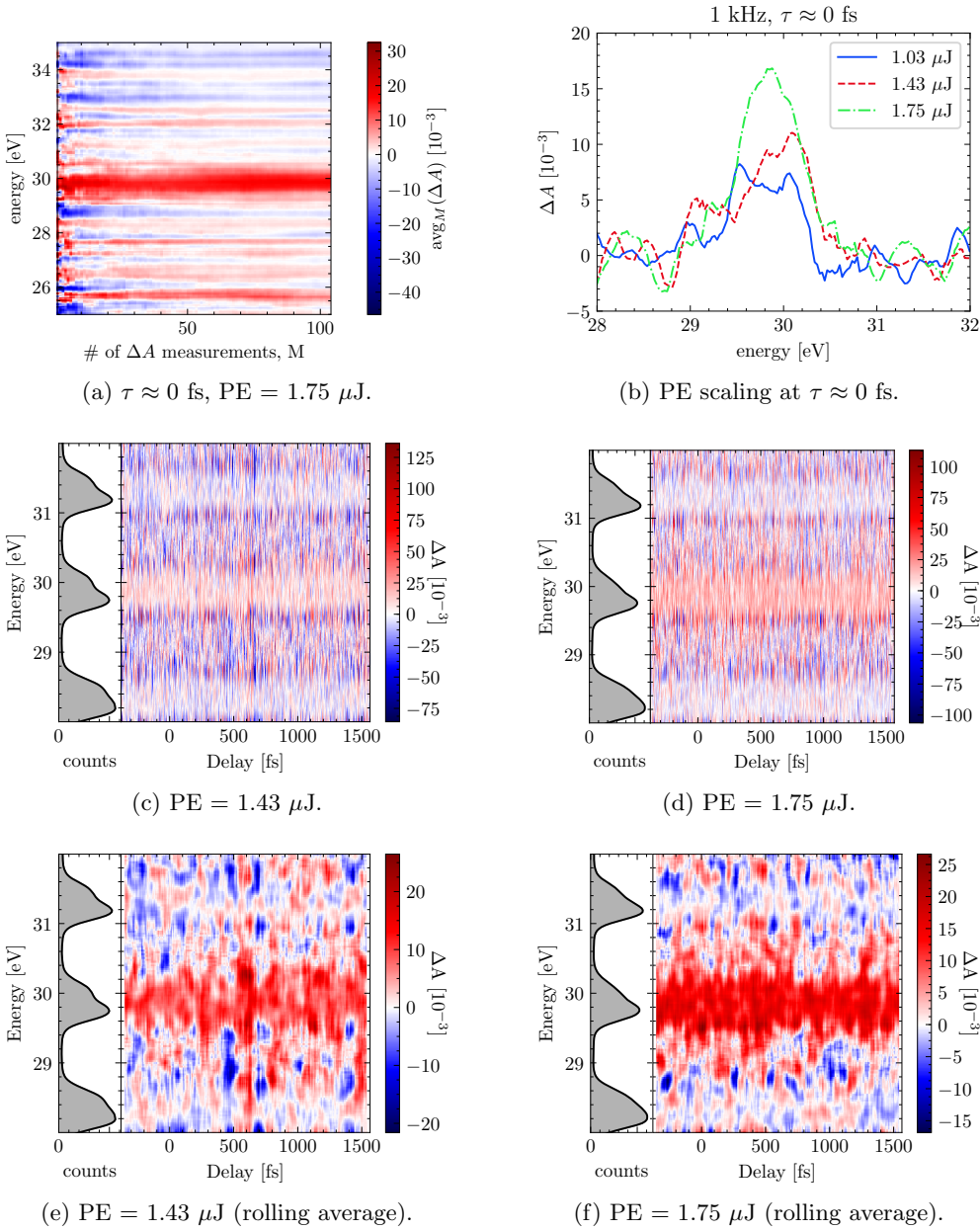


Figure 1.23: 1 kHz ATAS measurements in Ge using a  $\lambda = 1450$  nm excitation pulse. Fig. 1.23a: fixed-delay ATAS measurements with a pulse energy of 1.75  $\mu\text{J}$ . Fig. 1.23b: Pulse energy scaling at overlap of 1 kHz measurements. Figs. 1.23c to 1.23f: delay scans at 1 kHz. Figs. 1.23c and 1.23d: raw delay scan data. Figs. 1.23e and 1.23f: rolling average of the raw data with a 65 fs window (20 delay points). The left panel on each spectrogram shows the ground state spectrum  $S_{gs}(E)$ . See text for details.

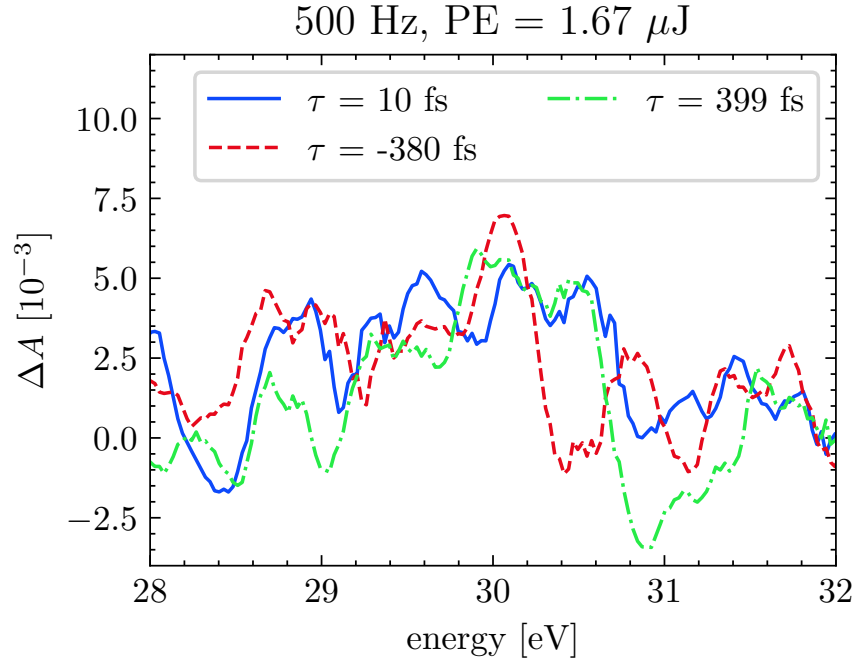


Figure 1.24: 500 Hz ATAS measurements in Ge using a  $\lambda = 1450$  nm,  $1.67 \mu\text{J}$  excitation pulse. Each delay curve is an average of 104 identical measurements. The sample shows no delay dependence within the uncertainty of the measurement.

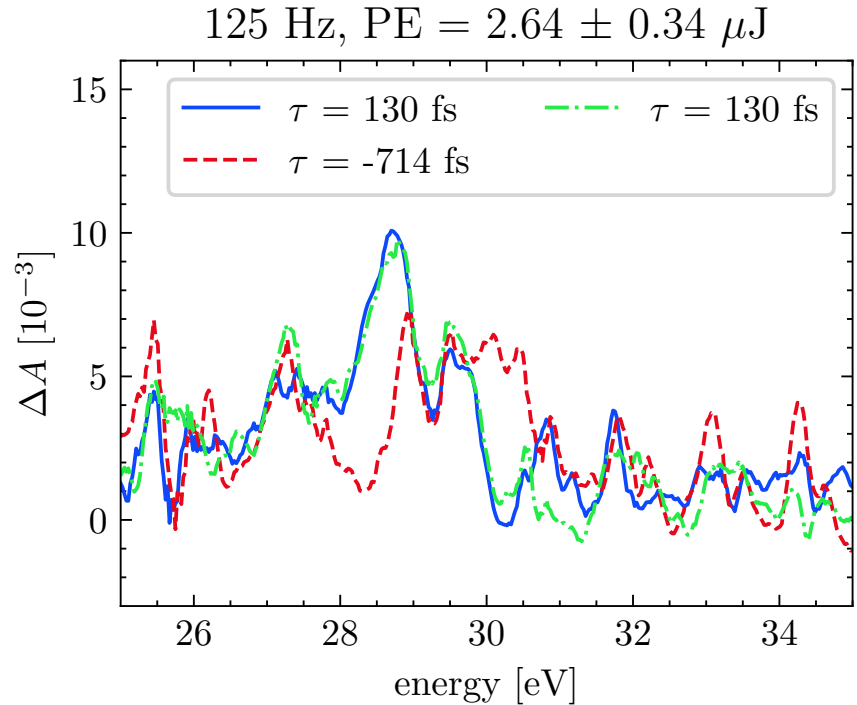


Figure 1.25: 125 Hz ATAS measurements in Ge using a  $\lambda = 1450$  nm,  $2.64 \mu\text{J}$  excitation pulse. Each lineout represents the average of 394 measurements. See text for details.

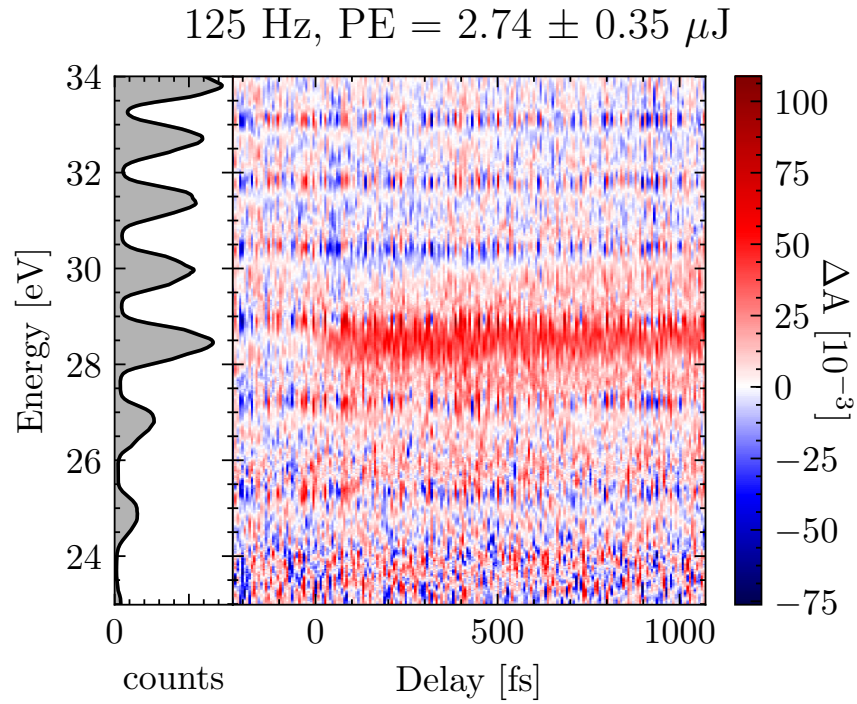


Figure 1.26: 125 Hz delay scan in Ge using a  $\lambda = 1450$  nm,  $2.74 \pm 0.35 \mu\text{J}$  excitation pulse. This is an average of 3 repeated measurements. See text for details.

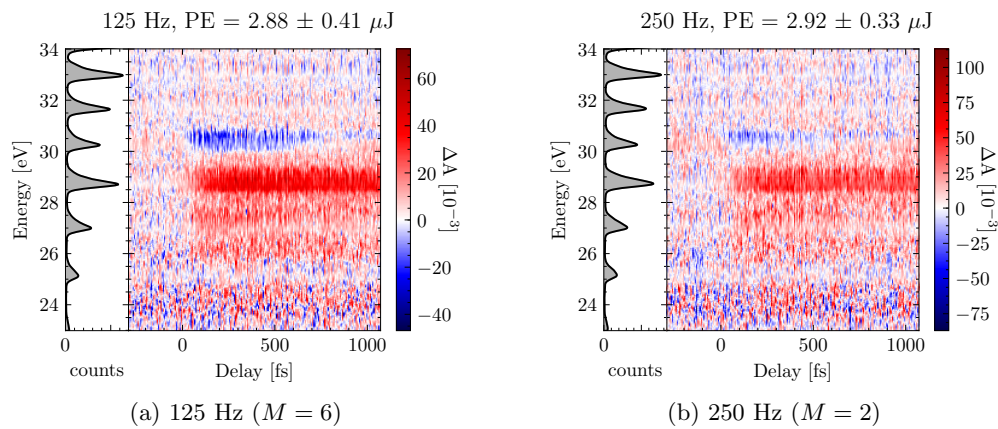


Figure 1.27: 125 vs. 250 Hz measurements at  $\lambda = 1430$  nm.

One possible origin of a delay-independent signal can be a very long-lived excited state with lifetime  $1/\Gamma$ . Each laser shot initiates an assortment of electron and phonon dynamics, each with their own time scales. If any of these excited states have time scales that approach the inverse rep. rate of the laser ( $1/RR$ ), then the dynamics from the previous shot will still be evolving by time the next shot arrives. Since each exposure integrates over hundreds or thousands of laser shots, measurements at a nominal delay  $\tau$  will contain information from several delays  $\tau_i$ , each separated by the time between laser shots:  $\tau_i = \tau, \tau - \frac{1}{RR}, \tau - \frac{2}{RR}, \dots$ , with the amplitude of each contribution weighed by an exponential decay factor  $\exp(+\tau_i\Gamma)$ . If this is the case, then the magnitude of the delay-independent signal should decrease as time between laser shots is increased. As the time between laser shots is increased past the lifetime of the state, the excited state population from the previous laser shot will be small enough to observe the dynamics of the shorter-lived states. Experimentally, we can accomplish this by adjusting the rep. rate divider on the Spitfire amplifier (which reduces the rep. rate), and/or using an optical chopper.

The rep. rate was halved to 500 Hz using the Spitfire's rep. rate divider ( $m = 2$ ) and the exposure time was doubled to 1 second so that the number of laser shots per exposure was held constant. A series of fixed-delay measurements were recorded using a  $1.67 \mu\text{J}$  pulse energy, shown in Fig. 1.24. The spectral feature at 30 eV is still present, but it does not exhibit any delay dependence within the uncertainty of the measurement. It is notable that, for a similar pulse energy, the magnitude of the feature at 500 Hz is half that of the 1 kHz measurement. This is consistent with the hypothesis of a long-lived state contributing to the signal.

The rep. rate was lowered to 125 Hz using a combination of the rep. rate divider ( $m = 4$ ) and an optical chopper ( $T = 50\%$ ) placed after the TOPAS. The exposure time was increased to 4 seconds to maintain sufficient counts on the detector. An ATAS spectrum was recorded about 130 fs after temporal overlap and several hundred fs before overlap using a  $2.64 \pm 0.34 \mu\text{J}$  excitation pulse ( $\lambda = 1450 \text{ nm}$ ), as shown in Fig. 1.25. A second measurement after overlap was recorded to ensure repeatability. At negative delays (red curve), we see the familiar 30 eV feature, albeit weaker at  $6 \times 10^{-3}$ . Near overlap, we see a new feature

emerge at 28.7 eV, with a magnitude of  $\approx 10 \times 10^{-3}$ . This observation is consistent with long-lived excited state at 30 eV. A delay scan at 125 Hz, shown in Fig. 1.26, reveals that the 28.7 eV feature is indeed time-dependent with a ps-scale lifetime.

The fundamental wavelength was decreased by 20 nm to 1430 nm, where the absorption length in Ge is about 5% shorter. For a fixed pulse energy, this increases the excitation fraction and thus the strength of the  $\Delta A$  signal. Changing the wavelength also changes which initial and final states near the Fermi level are populated, according to the band structure calculations in Fig. 1.11. Using this shorter wavelength we can observe a more robust sample response, as shown in Fig. 1.27.

At 1430 nm, we can see a sample response from 25.7 to 31 eV. From 25.7 to 30 eV, there is a broad increase in absorption, with the largest increase occurring between 28.4 and 29.5 eV. A decrease in absorption occurs between 30 and 31 eV. These features are present in both the 125 and 250 Hz data. The 30 eV negative delay feature persists in the 250 Hz dataset, but at  $12 \times 10^{-3}$  it does not overwhelm the rest of the sample response. Further measurements were performed at either 125 Hz to suppress the static feature, or at 250 Hz to minimize data collection time.

## Two-Color Generation

Under the HHG conditions used up until now, the XUV spectrum has been a comb of even harmonics separated in energy by  $2\hbar\omega \approx 1.7$  eV. This periodic spectral structure is the origin of a persistent systemic noise in our experiments. Owing to the extremely nonlinear nature of the HHG process, the yield of the harmonic spectrum randomly fluctuates throughout the experiment, with the largest modulations occurring on the “blue” (high energy) side of each harmonic peak. This results in a random fluctuation of  $\Delta A$  that oscillates about its true value. Additionally, the XUV flux approaches zero in the “valleys” between two harmonics. This is because the spectrometer has non-zero dark counts and can measure false counts due to various physical processes such as MCP arcing or stray light. In the low-flux regions of the spectrum, these noise sources can constitute a significant portion of the measured signal, which will further skew  $\Delta A$  away from its true value.

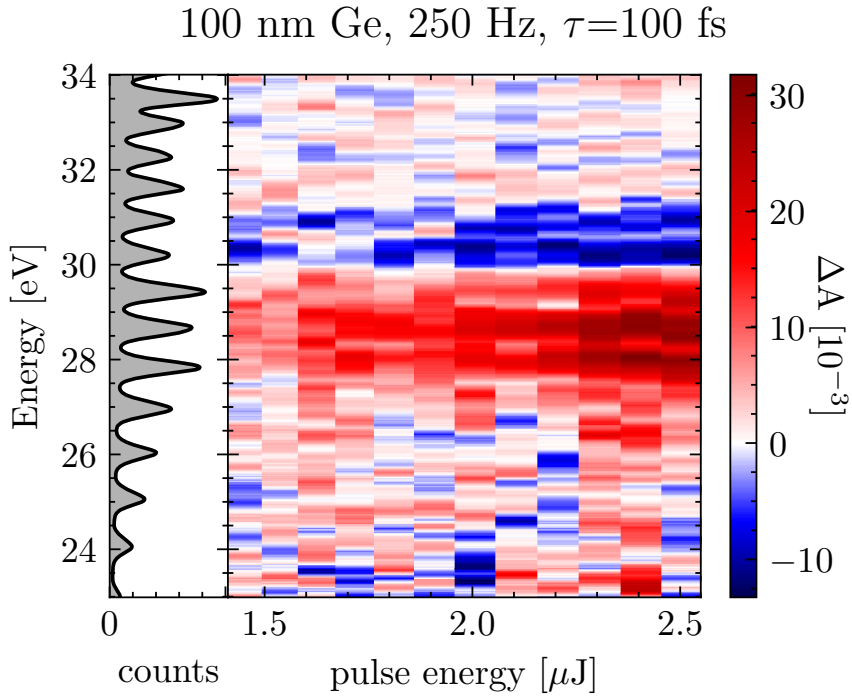


Figure 1.28: Pulse energy scan of 100 nm germanium sample near temporal overlap using a  $\lambda = 1430$  nm excitation pulse. Left panel shows the average ground state spectrum,  $S_{gs}(E)$  that results from two-color generation. Right panel shows the change in absorbance,  $\Delta A(E, PE)$ , as a function of pulse energy,  $PE$ . Data shown in this figure is the average of 20 identical measurements: individual datasets were background subtracted and normalized for exposure time before being averaged; no additional data processing was performed on this dataset. See text for details.

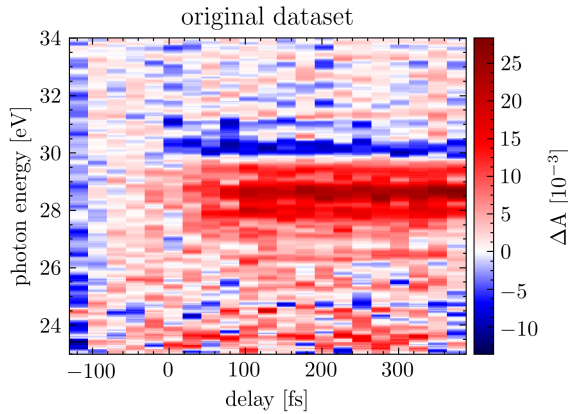


Figure 1.29: Average of 50 ATAS experiments using optimized experimental parameters. No corrections have been made to the data. See text for details.

Many of these artifacts are intrinsic to any experiment uses a harmonic comb and is sensitive to the amplitude of the XUV spectrum. This noise is visible in all of our experiments, but it is most apparent in Fig. 1.26. In this figure, we see horizontal bands separated by  $2\hbar\omega$ , centered on the blue side of each harmonic and oscillating around zero. In Fig. 1.27, we can see a  $2\omega$  modulation in  $\Delta A$  in the region 26 - 28 eV, with  $\Delta A$  approaching zero in the valleys where the XUV flux approaches zero. As described above, these features are artifacts of the XUV spectrum and the detection method.

This noise can be eliminated by using an isolated attosecond pulse (IAP), which produces a continuum in the spectral domain. However, our lab does not possess this capability. Instead we utilize two-color generation, which creates a harmonic comb with spacing  $\omega \approx 0.87$  eV that effectively doubles the spectral content of the XUV light. This method generates harmonics in the gas medium from the coherent sum of spatially- and temporally-overlapped  $\omega$  and  $2\omega$  fields. This was achieved by placing a BBO crystal, 200  $\mu\text{m}$  of calcite and a zero order 1310 nm  $\lambda/2$  waveplate between L3 and the generation chamber vacuum window. Two-color generation has the added benefit of changing the XUV spectrum without altering the IR pump arm characteristics.

The two-color generation XUV spectrum is shown in the left panel of Fig. 1.28. Compared to the spectra in Fig. 1.27, the two-color generation spectrum is twice as dense and provides much better spectral coverage of the transient absorption feature. Under these generation conditions, a pulse energy scan was performed as shown in the right panel of this figure. The pulse energy range is bounded by the detection threshold of the spectrometer on the lower end and the sample damage threshold on the higher end. In Fig. 1.28, we can see two distinct spectral features emerge from the noise as the pulse energy is increased. We see two features emerge from the noise and grow steadily brighter with increasing pulse energy. However, even with two-color generation and the maximum signal at PE = 2.5  $\mu\text{J}$ , a faint  $\omega$  modulation appears in the  $\Delta A$  signal.

With the experimental conditions optimized, we performed a series of delay scans on a 100 nm Ge sample. The experimental parameters are as follows. Harmonics were generated via two-color generation using a fundamental wavelength of  $\lambda = 1430$  nm and a rep rate

of 125 Hz. The IR excitation pulse energy (measured before L4) was  $2.85 \mu\text{J}$ . The camera was set to an exposure time of 3 seconds with an MCP voltage of +2200 VDC. To vary the delay, the wedges were moved in  $190 \mu\text{m}$  steps, corresponding to a step size of  $\approx 24.7 \text{ fs}$  over the range  $\tau = -120 \rightarrow +390 \text{ fs}$ . The sample was rastered laterally through the XUV focus between each delay point with a step size of  $200 \mu\text{m}$ . Each delay measurement consisted of 22 delay points, which took approximately 6 minutes to acquire. The delay measurement was repeated back-to-back for a total of 50 runs over the course of 5 hours. Subsequent delay measurements were done using the same raster points as the previous delay measurement, providing a one-to-one mapping of delay-to-spatial position on the sample. The pulse energy was monitored throughout the experiment using a photodiode (PD in Fig. 1.1); the pulse energy over the course of the experimental run had a relative stability of 1.8% (std/avg). These results are shown in Fig. 1.29. Additional processing needs to be done to this dataset before it can be analyzed, which will be discussed in the next chapter.

## 1.10 Summary

In summary, the concept of an attosecond transient absorption spectroscopy measurement (ATAS) and the experimental equipment used were briefly introduced. Requirements on the physical dimensions and electronic structure of the sample were discussed, along with the detection geometry and the relative contribution of the real and imaginary parts of the refractive index.

Numerical simulations of the interaction intensity were performed, and the carrier excitation fraction as a function of input pulse energy was estimated. Practical considerations involving the importance of the spatial overlap were detailed, and the experimental conditions for a prototypical long-wavelength ATAS measurement in germanium were optimized. By the end of this chapter we have collected the ATAS experimental data, but it remains too noisy to analyze. In the following chapter, we will develop methods to systematically clean the data in preparation for physical interpretation.

## BIBLIOGRAPHY

- [1] D. R. Austin, K. R. P. Kafka, Y. H. Lai, Z. Wang, C. I. Blaga, and E. A. Chowdhury. Femtosecond laser damage of germanium from near- to mid-infrared wavelengths. *Opt. Lett., OL*, 43(15):3702–3705, Aug. 2018.
- [2] Y.-H. Chiu, N. G. Minutillo, R. E. Williams, G. J. Smith, D. W. McComb, J. A. Carlin, E. Johnston-Halperin, and F. Yang. Photoluminescence evolution in GaAs/AlGaAs core/shell nanowires grown by MOCVD: Effects of core growth temperature and substrate orientation. *Journal of Crystal Growth*, 429:1–5, Nov. 2015.
- [3] A. Cirri, J. Husek, S. Biswas, and L. R. Baker. Achieving Surface Sensitivity in Ultrafast XUV Spectroscopy: M<sub>2,3</sub>-Edge Reflection–Absorption of Transition Metal Oxides. *J. Phys. Chem. C*, 121(29):15861–15869, July 2017.
- [4] S. K. Cushing, A. Lee, I. J. Porter, L. M. Carneiro, H.-T. Chang, M. Zürch, and S. R. Leone. Differentiating Photoexcited Carrier and Phonon Dynamics in the  $\Delta$ ,  $L$ , and  $\Gamma$  Valleys of Si(100) with Transient Extreme Ultraviolet Spectroscopy. *J. Phys. Chem. C*, 123(6):3343–3352, Feb. 2019.
- [5] E. G. Gamaly, A. V. Rode, B. Luther-Davies, and V. T. Tikhonchuk. Ablation of solids by femtosecond lasers: Ablation mechanism and ablation thresholds for metals and dielectrics. *Physics of Plasmas*, 9(3):949–957, Feb. 2002.
- [6] E. Gullikson. CXRO X-Ray Interactions With Matter.  
[http://henke.lbl.gov/optical\\_constants/](http://henke.lbl.gov/optical_constants/).

- [7] M. Harb, R. Ernstorfer, T. Dartigalongue, C. T. Hebeisen, R. E. Jordan, and R. J. D. Miller. Carrier Relaxation and Lattice Heating Dynamics in Silicon Revealed by Femtosecond Electron Diffraction. *J. Phys. Chem. B*, 110(50):25308–25313, Dec. 2006.
- [8] C. J. Kaplan, P. M. Kraus, A. D. Ross, M. Zürch, S. K. Cushing, M. F. Jager, H.-T. Chang, E. M. Gullikson, D. M. Neumark, and S. R. Leone. Femtosecond tracking of carrier relaxation in germanium with extreme ultraviolet transient reflectivity. *Phys. Rev. B*, 97(20):205202, May 2018.
- [9] L. Keldysh. Ionization in the Field of a Strong Electromagnetic Wave. *SOVIET PHYSICS JETP*, 20:1307–1314, May 1965.
- [10] E. Nichelatti. Complex refractive index of a slab from reflectance and transmittance: Analytical solution. *J. Opt. A: Pure Appl. Opt.*, 4(4):400–403, July 2002.
- [11] T. N. Nunley, N. S. Fernando, N. Samarasinha, J. M. Moya, C. M. Nelson, A. A. Medina, and S. Zollner. Optical constants of germanium and thermally grown germanium dioxide from 0.5 to 6.6eV via a multisample ellipsometry investigation. *Journal of Vacuum Science & Technology B, Nanotechnology and Microelectronics: Materials, Processing, Measurement, and Phenomena*, 34(6):061205, Nov. 2016.
- [12] M. Schultze, K. Ramasesha, C. D. Pemmaraju, S. A. Sato, D. Whitmore, A. Gandman, J. S. Prell, L. J. Borja, D. Prendergast, K. Yabana, D. M. Neumark, and S. R. Leone. Attosecond band-gap dynamics in silicon. *Science*, 346(6215):1348–1352, Dec. 2014.
- [13] G. Vdovin, F. van Goor, and Guyskk. LightPipes for Python. Flexible Optical.
- [14] M. Volkov, S. A. Sato, F. Schlaepfer, L. Kasmi, N. Hartmann, M. Lucchini, L. Gallmann, A. Rubio, and U. Keller. Attosecond screening dynamics mediated by electron localization in transition metals. *Nat. Phys.*, pages 1–5, Aug. 2019.
- [15] M. Zürch, H.-T. Chang, L. J. Borja, P. M. Kraus, S. K. Cushing, A. Gandman, C. J. Kaplan, M. H. Oh, J. S. Prell, D. Prendergast, C. D. Pemmaraju, D. M. Neumark,

- and S. R. Leone. Direct and simultaneous observation of ultrafast electron and hole dynamics in germanium. *Nat Commun*, 8(1):15734, Aug. 2017.
- [16] M. Zürch, H.-T. Chang, P. M. Kraus, S. K. Cushing, L. J. Borja, A. Gandman, C. J. Kaplan, M. H. Oh, J. S. Prell, D. Prendergast, C. D. Pemmaraju, D. M. Neumark, and S. R. Leone. Ultrafast carrier thermalization and trapping in silicon-germanium alloy probed by extreme ultraviolet transient absorption spectroscopy. *Structural Dynamics*, 4(4):044029, July 2017.